

TOI-1696: a nearby M4 dwarf with a $3R_{\oplus}$ planet in the Neptunian desert

MAYUKO MORI , JOHN H. LIVINGSTON , JEROME DE LEON , NORIO NARITA ,
TERUYUKI HIRANO , AKIHIKO FUKUI , KAREN A. COLLINS , NAHO FUJITA ,
YASUNORI HORI , HIROYUKI TAKO ISHIKAWA , KYOYE KAWAUCHI ,
KEIVAN G. STASSUN , NORIHARU WATANABE , STEVEN GIACALONE , REBECCA GORE,
ASHLEY SCHROEDER,¹² COURTNEY D. DRESSING , ALLYSON BIERYLA , ERIC L. N. JENSEN ,
BOB MASSEY , AVI SHPORER , MASAYUKI KUZUHARA , DAVID CHARBONNEAU ,
DAVID R. CIARDI , JOHN P. DOTY,¹⁹ EMMA ESPARZA-BORGES , HIROKI HARAKAWA,
KLAUS HODAPP , MASAHIRO IKOMA , KAI IKUTA , KEISUKE ISOGAI ,
JON M. JENKINS , TAIKI KAGETANI , TADAHIRO KIMURA,²⁴ TAKANORI KODAMA ,
TAKAYUKI KOTANI,^{2,3,6} VIGNESHWARAN KRISHNAMURTHY , TOMOYUKI KUDO ,
SEIYA KURITA,²⁴ TAKASHI KUROKAWA,^{2,25} NOBUHIKO KUSAKABE , DAVID W. LATHAM ,
BRIAN MCLEAN,²⁶ FELIPE MURGAS , JUN NISHIKAWA , TAKU NISHIUMI ,
MASASHI OMIYA,^{2,3} HUGH P. OSBORN , ENRIC PALLE , HANNU PARVIAINEN ,
GEORGE R. RICKER , SARA SEAGER , TAKUMA SERIZAWA,^{25,3} MOTOHIDE TAMURA ,
HUAN-YU TENG , YUKA TERADA , JOSEPH D. TWICKEN , AKITOSHI UEDA,^{2,3,6}
ROLAND VANDERSPEK , SÉBASTIEN VIEVARD,^{20,2} JOSHUA N. WINN , AND YUJIE ZOU 

¹ Department of Astronomy, Graduate School of Science, The University of Tokyo, 7-3-1 Hongo, Bunkyo, Tokyo 113-0033, Japan

² Astrobiology Center, 2-21-1 Osawa, Mitaka, Tokyo 181-8588, Japan

³ National Astronomical Observatory of Japan, 2-21-1 Osawa, Mitaka, Tokyo 181-8588, Japan

⁴ Komaba Institute for Science, The University of Tokyo, 3-8-1 Komaba, Meguro, Tokyo 153-8902, Japan

⁵ Instituto de Astrofísica de Canarias (IAC), 38205 La Laguna, Tenerife, Spain

⁶ Department of Astronomy, School of Science, The Graduate University for Advanced Studies (SOKENDAI), 2-21-1 Osawa, Mitaka, Tokyo, Japan

⁷ Center for Astrophysics | Harvard & Smithsonian, 60 Garden Street, Cambridge, MA 02138, USA

⁸ Department of Astronomy, Kyoto University, Kitashirakawa-Oiwake-cho, Sakyo-ku, Kyoto 606-8502, Japan

⁹ Departamento de Astrofísica, Universidad de La Laguna (ULL), 38206 La Laguna, Tenerife, Spain

¹⁰ Department of Physics and Astronomy, Vanderbilt University, Nashville, TN 37235, USA

¹¹ Department of Multi-Disciplinary Sciences, Graduate School of Arts and Sciences, The University of Tokyo, 3-8-1 Komaba, Meguro, Tokyo 153-8902, Japan

¹² Department of Astronomy, University of California Berkeley, Berkeley, CA 94720, USA

¹³ Department of Astronomy, The University of California, Berkeley, CA 94720, USA

¹⁴ Department of Physics & Astronomy, Swarthmore College, Swarthmore PA 19081, USA

¹⁵ Villa '39 Observatory, Landers, CA 92285, USA

¹⁶ Department of Physics and Kavli Institute for Astrophysics and Space Research, Massachusetts Institute of Technology, Cambridge, MA 02139, USA

¹⁷ Harvard-Smithsonian Center for Astrophysics, 60 Garden St, Cambridge, MA 02138, USA

¹⁸ Caltech/IPAC-NASA Exoplanet Science Institute, 770 S. Wilson Avenue, Pasadena, CA 91106, USA

¹⁹ Noqsi Aerospace Ltd., 15 Blanchard Avenue, Billerica, MA 01821, USA

²⁰ Subaru Telescope, 650 N. Aohoku Place, Hilo, HI 96720, USA

²¹ University of Hawaii, Institute for Astronomy, 640 N. Aohoku Place, Hilo, HI 96720, USA

²² Okayama Observatory, Kyoto University, 3037-5 Honjo, Kamogatacho, Asakuchi, Okayama 719-0232, Japan

²³ NASA Ames Research Center, Moffett Field, CA 94035, USA

⁴⁵ ²⁴Department of Earth and Planetary Science, Graduate School of Science, The University of Tokyo, 7-3-1 Hongo,
⁴⁶ Bunkyo, Tokyo 113-0033, Japan

⁴⁷ ²⁵Institute of Engineering, Tokyo University of Agriculture and Technology, 2-24-16, Naka-cho, Koganei, Tokyo,
⁴⁸ 184-8588, Japan

⁴⁹ ²⁶Space Telescope Science Institute, 3700 San Martin Drive, Baltimore, MD, 21218, USA

⁵⁰ ²⁷NCCR/Planet-S, Universität Bern, Gesellschaftsstrasse 6, 3012 Bern, Switzerland

⁵¹ ²⁸Department of Earth, Atmospheric, and Planetary Sciences, Massachusetts Institute of Technology, Cambridge,
⁵² MA 02139, USA

⁵³ ²⁹Department of Aeronautics and Astronautics, Massachusetts Institute of Technology, Cambridge, MA 02139, USA
⁵⁴ ³⁰Department of Earth and Planetary Sciences, School of Science, Tokyo Institute of Technology, 2-12-1 Ookayama,
⁵⁵ Meguro-ku, Tokyo 152-8551, Japan

⁵⁶ ³¹Institute of Astronomy and Astrophysics, Academia Sinica, P.O. Box 23-141, Taipei 10617, Taiwan, R.O.C.
⁵⁷ Department of Astrophysics, National Taiwan University, Taipei 10617, Taiwan, R.O.C.

⁵⁸ ³²SETI Institute, Mountain View, CA 94043, USA

⁵⁹ ³³Department of Astrophysical Sciences, Princeton University, 4 Ivy Lane, Princeton, NJ 08544, USA

(Received March 3, 2022)

Submitted to ApJ

ABSTRACT

We present the discovery and validation of a temperate sub-Neptune around the nearby mid-M dwarf TIC 470381900 (TOI-1696), with a radius of $3.09 \pm 0.11 R_{\oplus}$ and an orbital period of 2.5 days, using a combination of *TESS* and follow-up observations using ground-based telescopes. Joint analysis of multi-band photometry from *TESS*, MuSCAT, MuSCAT3, Simistro, and KeplerCam confirmed the transit signal to be achromatic as well as refined the orbital ephemeris. High-resolution imaging with Gemini/'Alopeke and high-resolution spectroscopy with the Subaru/IRD confirmed that there are no stellar companions or background sources to the star. The spectroscopic observations with IRD and IRTF/SpeX were used to determine the stellar parameters, and found the host star is an M4 dwarf with an effective temperature of $T_{\text{eff}} = 3185 \pm 76$ K and a metallicity of $[\text{Fe}/\text{H}] = 0.336 \pm 0.060$ dex. The radial velocities measured from IRD set a 2σ upper limit on the planetary mass to be $48.8 M_{\oplus}$. The large radius ratio ($R_p/R_{\star} \sim 0.1$) and the relatively bright NIR magnitude (J=12.2 mag) make this planet an attractive target for further followup observations. TOI-1696 b is one of the planets belonging to the Neptunian desert with the highest transmission spectroscopy metric discovered to date, making it an interesting candidate for atmospheric characterizations with *JWST*.

Keywords: Exoplanet astronomy (486) – M dwarf stars (982) – Speckle interferometry (1552) – Transit photometry (1709) – High resolution spectroscopy (2096)

1. INTRODUCTION

Exoplanet population statistics from the *Kepler* mission (Borucki et al. 2010) revealed that there is a dearth of planets around the size of Neptune ($\sim 3\text{--}4 R_{\oplus}$) with orbital periods less than 2–4 d. This has been referred to as the “Neptunian Desert” or “photo-evaporation desert” or simply “evaporation desert” (Szabó & Kiss 2011; Mazeh et al. 2016; Lopez 2017). The scarcity of planets in this region of parameter space can be explained by photo-evaporation, that is, atmospheric mass loss due to high-energy irradiation from the host star

(Owen & Wu 2017). The small number of planets that have so far been found in the desert (e.g. West et al. 2019; Jenkins et al. 2020) are believed to retain substantial atmospheres (or are still in the process of losing them), but the physical mechanisms are not well understood. Comparing planets that have lost their atmospheres with those that have retained their atmospheres will be useful to understand the processes such as photo-evaporation theory. Therefore, it is important to increase the number of planets in this region and reveal the nature of their atmospheres. *TESS* (Ricker et al.

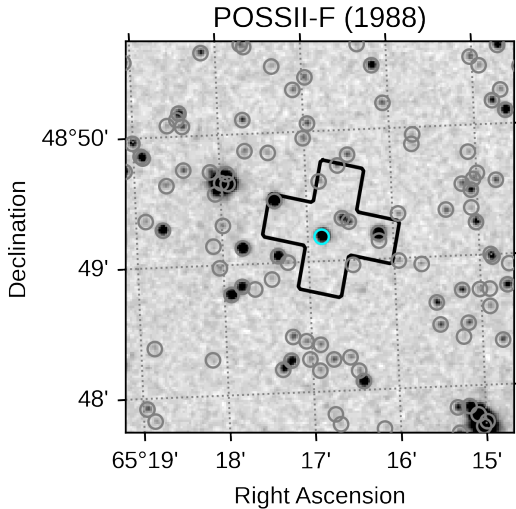


Figure 1. Archival imaging from POSSII-F survey (taken in 1998; Reid et al. 1991) with the *TESS* photometric aperture (black outline) and *Gaia* sources (gray circles). The cyan circle indicates the position of TOI-1696; we note the proper motion is low enough that its current position is not significantly offset in the archival image.

106 2015), which has identified over 5000 exoplanet
107 candidates so far¹, made it possible to discover
108 more planets in the Neptunian Desert.

109 In this paper, we report the validation of a
110 new planet around the mid-M dwarf TOI-1696,
111 whose transits were identified by the *TESS*
112 mission. The planet TOI-1696 b has a sub-
113 Neptune size ($3.09 \pm 0.11 R_{\oplus}$) and an orbital
114 period of 2.5 days, which places it within (or
115 near the boundaries of) the Neptunian desert.

116 The large radius ratio ($R_p/R_{\star} \sim 0.1$) makes
117 the planet's transits deep, and combined with
118 the relatively bright near-IR (NIR) magnitude
119 ($J=12.2$ mag) of the star, the planet is one of
120 the best targets for future atmospheric research
121 via transmission spectroscopy.

122 The rest of this paper is organized as follows.
123 In Section 2, we present the observational data
124 and the reduction procedures used for the anal-
125 yses. In Section 3, we explain the analyses
126 methods and results. In Section 4, we discuss
127 the features of the planet and its future obser-
128 vational prospects, concluding with a summary
129 in Section 5.

130 2. OBSERVATIONS & DATA REDUCTION

¹ As of 2022 February per <https://exoplanetarchive.ipac.caltech.edu/>

131 2.1. Transit photometry - *TESS*

132 *TESS* observed TOI-1696 with a 2 min ca-
133 dence in Sector 19 from 2019 Jul 25 to Aug
134 22, resulting in photometry spanning approxi-
135 mately 27 days with a gap of about one day in
136 the middle when the satellite reoriented itself
137 for data downlink near perigee. Light curves
138 were produced by the Science Processing Op-
139 erations Center (SPOC) photometry pipeline
140 (Jenkins 2002; Jenkins et al. 2010; Jenkins & et
141 al. 2020) using the aperture shown in Figure 1.
142 We used the PDCSAP light curves produced by
143 the SPOC pipeline (Stumpe et al. 2012; Smith
144 et al. 2012; Stumpe et al. 2014) for our tran-
145 sit analyses. TOI-1696 is located in a fairly
146 crowded field, owing to its low galactic lati-
147 tude ($b = -0.81^{\circ}$). The SPOC pipeline applies
148 a photometric dilution correction based on the
149 CROWDSAP metric, which we independently con-
150 firmed by computing dilution values based on
151 *Gaia* DR2 magnitudes².

152 TOI-1696.01 was detected by the SPOC
153 pipeline in a transiting planet search, and the
154 candidate was subsequently reported to the
155 community by the *TESS* Science Office (TSO)
156 on 2020 January 30 via the *TESS* Object of
157 Interest (TOI; Guerrero et al. (2021)) Releases
158 portal³. The candidate passed all data valida-
159 tion diagnostic tests (Twicken et al. 2018) per-
160 formed by the SPOC⁴. The SPOC pipeline re-
161 moved the transit signals of TOI-1696.01 from
162 the light curve and performed a search for ad-
163 ditional planet candidates (Li et al. 2019), but
164 none were reported.

165 We independently confirmed the transit sig-
166 nals found by the SPOC. After removing stel-
167 lar variability and residual instrumental sys-
168 tematics from the PDCSAP light curve using
169 a 2nd order polynomial Savitzky-Golay filter,
170 we searched for periodic transit-like signals us-
171 ing the transit least-squares algorithm (TLS;
172 Hippke & Heller 2019)⁵, resulting in the detec-
173 tion of TOI-1696.01 with a signal detection ef-
174 ficiency (SDE) of 11.6, a transit signal-to-noise

² approximating *Gaia* R_p as the *TESS* bandpass, and assuming a full width at half maximum (FWHM) of 25''

³ <https://tess.mit.edu/toi-releases/>

⁴ Full vetting report available for download at https://exo.mast.stsci.edu/exomast_planet.html?planet=TOI169601

⁵ <https://transitleastsquares.readthedocs.io/en/latest/index.html>

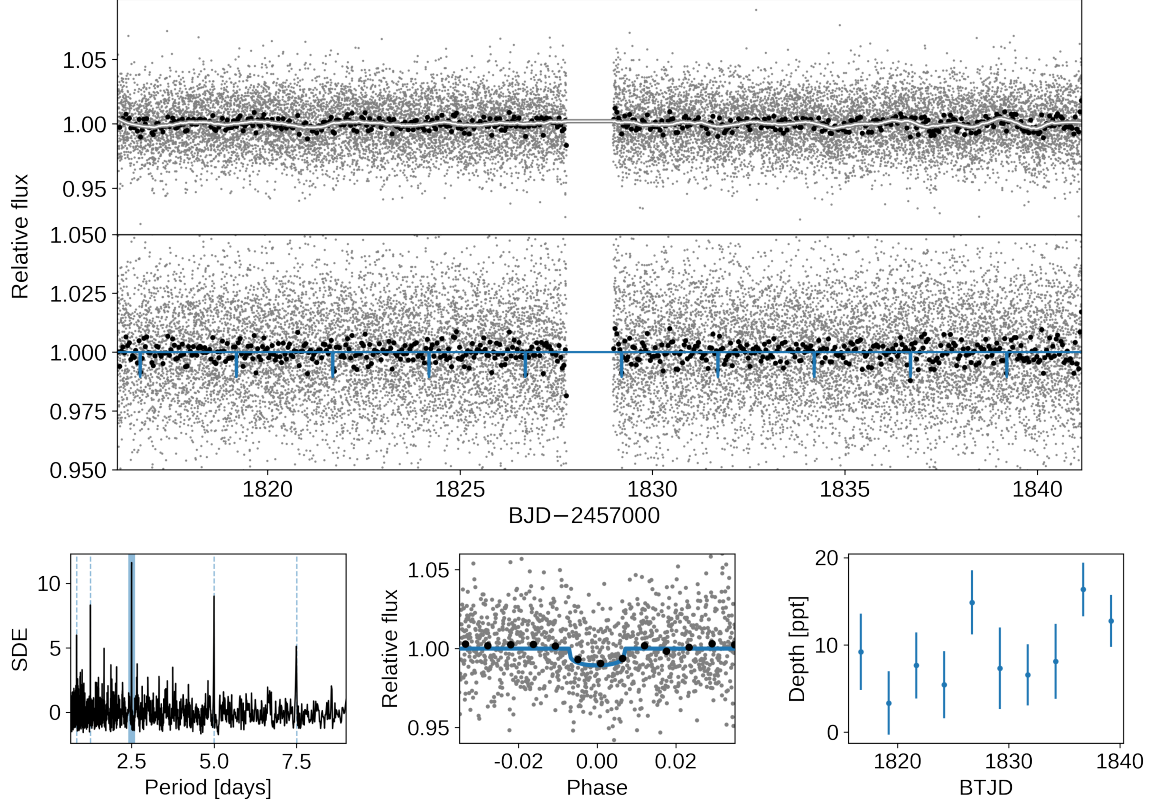


Figure 2. The upper panels show the *TESS* PDCCSAP lightcurve with Savitzky-Golay (window=1001) variability model (top), and the flattened lightcurve with TLS model (bottom). The lower panels show the TLS power spectrum (left), folded *TESS* lightcurve with TLS model (middle), and individual transit depths from TLS (right).

ratio (SNR) of 7.4, orbital period of 2.50031 ± 0.00001 days, and transit depth of 10.6 parts per thousand (ppt), which is consistent with the values reported by the *TESS* team on ExoFOP-TESS⁶. We subtracted this signal and repeated the transit search, but no additional signals with SDE above 10 were found. TLS also reports the approximate depths of each individual transit; we note that these transit depths and uncertainties are useful for diagnostic purposes only, as they are simplistically determined from the mean and standard deviation of the in-transit flux. The depths of the odd transits are within 1.5σ of the even transits, suggesting a low probability of either signal being caused by an eclipsing binary at twice the detected period. The TLS detection is shown in Figure 2.

2.2. Transit photometry - FLWO/KeplerCam

⁶ <https://exofop.ipac.caltech.edu/tess/>

We used KeplerCam, mounted on the 1.2m telescope located at the Fred Lawrence Whipple Observatory (FLWO) atop Mt. Hopkins, Arizona, to observe a full transit on 2020 February 17. KeplerCam has a $23' \times 23'$ field-of-view and operates in binned by 2 mode producing a pixel scale of $0.672''$. Images were obtained in the i-band with an exposure time of 300 seconds. A total of 29 images were collected over 144 minutes. The data were reduced using standard IDL routines and photometry was performed using the AstroImageJ software package (Collins et al. 2017).

2.3. Transit photometry - LCO/SINISTRO

We observed a full transit on 2020 November 13, using Sinistro, an optical camera mounted on a 1m telescope located at McDonald Observatory in Texas, operated by Las Cumbres Observatory (Brown et al. 2013). Sinistro has a $26' \times 26'$ field of view with a pixel scale of $0.389''$. We observed 62 images in total during 339 minutes, using a V-band filter, with an exposure time of 5 min. The data were reduced

217 by the standard LCOGT BANZAI pipeline (Mc-
 218 Cully et al. 2018), and photometry was per-
 219 formed using AstroImageJ software.

220 2.4. *Transit photometry - LCO/MuSCAT3*

221 MuSCAT3 is a multi-band simultaneous cam-
 222 era installed on the 2m Faulkes Telescope
 223 North at Las Cumbres Observatory (LCO) on
 224 Haleakala, Maui (Narita et al. 2020). It has
 225 four channels, enabling simultaneous photom-
 226 etry in the g (400–550 nm), r (550–700 nm),
 227 i (700–820 nm) and z_s (820–920 nm) bands.
 228 Each channel has a 2048×2048 pixel CCD cam-
 229 era with a pixel scale of $0.27''$, providing a
 230 $9'.1 \times 9'.1$ field of view. We observed a full
 231 transit of TOI-1696.01 on 2020 December 23,
 232 from BJD 2459206.703523 to 2459206.827246.
 233 We took 36, 41, 89, and 131 exposures with ex-
 234 posure times of 300, 265, 120, and 80 s in the
 235 g , r , i , and z_s bands, respectively.

236 The data reduction was conducted by the
 237 standard LCOGT BANZAI pipeline. Then the
 238 differential photometry was conducted by a
 239 customized aperture-photometry pipeline for
 240 MuSCAT series (Fukui et al. 2011). The op-
 241 timized aperture radii are 8, 6, 10, and 8 pix-
 242 els ($2.16''$, $1.62''$, $2.7''$, and $2.16''$) for the g , r ,
 243 i , and z_s bands, respectively. We optimized a
 244 set of comparison stars for each band to min-
 245 imize the dispersion of the light curves. For
 246 computational efficiency, and to achieve a more
 247 uniform signal-to-noise ratio (SNR), we subse-
 248 quently binned the g , r , i , and z_s data to 300,
 249 240, 180, and 120 s, respectively.

250 2.5. *Transit photometry - NAOJ* 251 *188cm/MuSCAT*

252 We also observed a full transit with MuS-
 253 CAT (Narita et al. 2015), which is installed
 254 on the 188cm telescope of National Astronomi-
 255 cal Observatory of Japan (NAOJ) in Okayama,
 256 Japan. MuSCAT has a similar optical de-
 257 sign as MuSCAT3 but has three CCD cam-
 258 eras for the g , r and z_s bands. On the night
 259 of 2021 July 28 we observed TOI-1696 from
 260 BJD 2459424.228358 to 2459424.30679. At
 261 that point, the r -band camera was not avail-
 262 able due to an instrumental issue, so we ob-
 263 served with only the g and z_s bands, using an
 264 exposure time of 60 s for both bands.

265 The data reduction and differential photome-
 266 try was performed using the pipeline described
 267 in Fukui et al. (2011). The optimized aperture

268 radii were 4 and 6 pixels ($1.44''$ and $2.16''$) for
 269 the g and z_s bands, respectively. Similarly to
 270 the MuSCAT3 data, we binned the g and z_s
 271 data to 300 and 120 s, respectively.

272 2.6. *Speckle imaging - Gemini/'Alopeke*

273 On the nights of 2020 December 03 and 2021
 274 October 14, TOI-1696 was observed with the
 275 'Alopeke speckle imager (Scott 2019), mounted
 276 on the 8.1 m Gemini North telescope on Mauna
 277 Kea. 'Alopeke simultaneously acquires data in
 278 two bands centered at 562 nm and 832 nm
 279 using high speed electron-multiplying CCDs
 280 (EMCCDs). We collected and reduced the
 281 data following the procedures described in
 282 Howell et al. (2011). The resulting recon-
 283 structed image achieved a contrast of $\Delta\text{mag} =$
 284 5.8 at a separation of $1''$ in the 832 nm band.
 285 No secondary sources were detected. The data
 286 taken on 2021 October 14 is shown in Figure 3.

287 2.7. *Adaptive optics imaging -* 288 *Palomar/PHARO*

289 On 2021 September 19 we conducted near-
 290 infrared high-resolution imaging using the
 291 adaptive optics instrument PHARO mounted
 292 on the 5 m Hale telescope at Palomar Obser-
 293 vatory (Hayward et al. 2001). We observed
 294 TOI-1696 separately in the $\text{Br}\gamma$ ($2.18 \mu\text{m}$) and
 295 H_{cont} ($2.29 \mu\text{m}$) bands, reaching a contrast of
 296 $\Delta\text{mag} = 8$ at a separation of $1''$ in both bands.
 297 The AO images and corresponding contrast
 298 curves are shown in Figure 4.

299 2.8. *High-resolution spectroscopy -* 300 *Subaru/IRD*

301 We obtained high-resolution spectra of TOI-
 302 1696 in the NIR with IRD (Tamura et al. 2012;
 303 Kotani et al. 2018), mounted on the 8.2 m
 304 Subaru telescope. IRD can achieve a spec-
 305 tral resolution of $\sim 70,000$ in the wavelength
 306 range 930 nm to 1740 nm. The derived spectra
 307 were used for the three purposes: to search for
 308 spectral companions (e.g. SB2 scenarios), to
 309 measure fundamental stellar parameters (e.g.
 310 effective temperature and metallicity), and to
 311 rule out large radial velocity (RV) variations
 312 that would indicate an eclipsing binary (EB),
 313 as well as placing a limit on the mass of the
 314 planet. From UT 2021 January 30 to 2022
 315 January 08, we obtained 13 spectra of TOI-
 316 1696 using 1800 s exposure times, as part of a
 317 Subaru Intensive Program (Proposal IDs S20B-

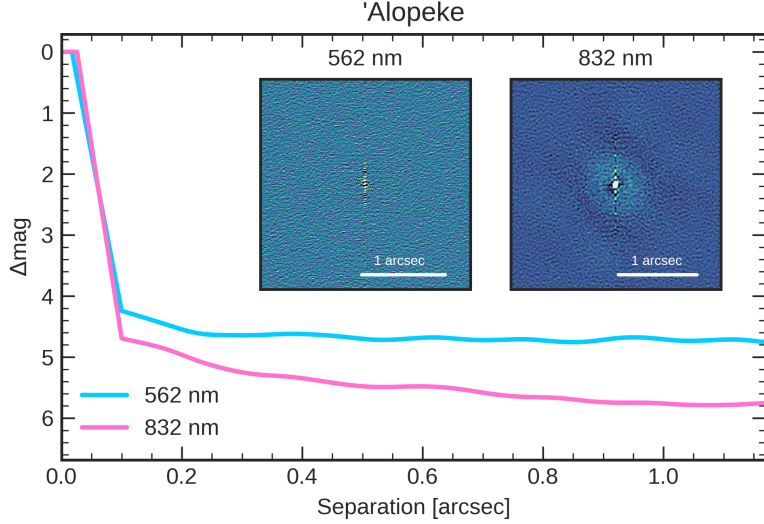


Figure 3. Gemini/'Alopeke reconstructed images and contrast curves produced as described in Section 2.6.

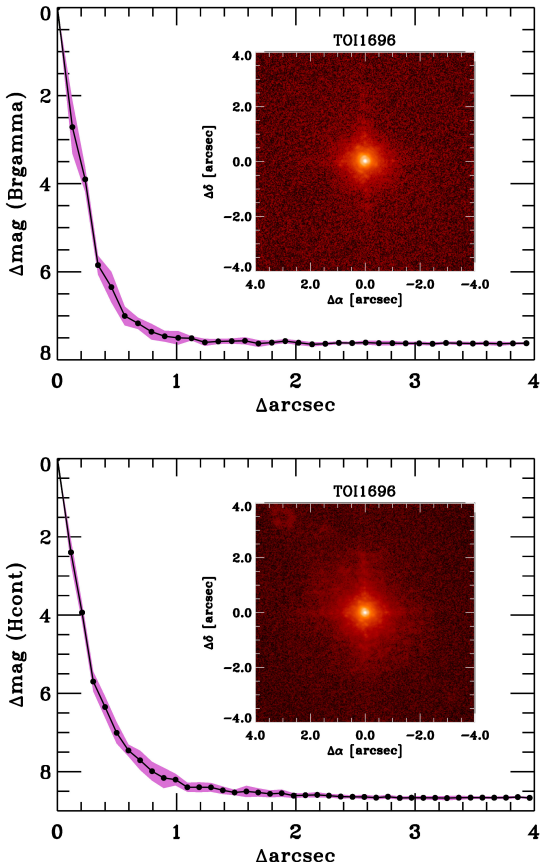


Figure 4. Palomar/PHARO images and contrast curves (top: Br γ ; bottom: H $_{\text{cont}}$) produced as described in Section 2.7.

088I and S21B-118I). The raw data were reduced using **IRAF** (Tody 1993) as well as a pipeline for the detector's bias processing and

wavelength calibrations developed by the IRD instrument team (Kuzuhara et al. 2018; Hirano et al. 2020). For the RV analyses and stellar parameter derivation, we computed a high-SNR coadded spectrum of the target following the procedures described in Hirano et al. (2020). For use as a spectral template in the analysis described in Section 3.2, we also downloaded archival IRD data of GJ 699 (Barnard's Star)⁷, which was obtained on 2019 March 23 (HST). We reduced and calibrated the GJ 699 data following the same procedures as the TOI-1696 data.

2.9. Medium-resolution spectroscopy - IRTF/SpeX

We collected observations of TOI-1696 on UT 2020 December 09 using SpeX, a medium-resolution spectrograph on the NASA Infrared Telescope Facility (IRTF) on Maunakea (Rayner et al. 2003). We obtained our observations in SXD mode with a $0.^{\prime}3 \times 15.^{\prime\prime}$ slit, providing a spectral resolution of $R \approx 2000$ over a wavelength range 700 nm to 2550 nm. In order to remove sky background and reduce systematics, the spectra were collected using an ABBA nod pattern (with a separation of $7.^{\prime}5$ between the A and B positions) and with the slit synced to the parallactic angle. We reduced our spectra using the **SpeXtool** reduction pipeline (Cushing et al. 2004) and removed

⁷ Using the Subaru-Mitaka-Okayama-Kiso-Archive (SMOKA)

³⁵¹ telluric contamination using `xteLLcor` (Vacca
³⁵² et al. 2003). The derived spectra were used to
³⁵³ calculate the stellar metallicity.

³⁵⁴ 3. ANALYSES & RESULTS

³⁵⁵ 3.1. *Stellar parameters estimation*

³⁵⁶ In the next subsections we estimate the
³⁵⁷ fundamental stellar parameters of TOI-1696.
³⁵⁸ First, the stellar effective temperature T_{eff} and
³⁵⁹ metallicity [Fe/H] are derived from two inde-
³⁶⁰ pendent methods; one is from the IRD spectra
³⁶¹ and the other is from the SpeX spectra and
³⁶² photometric relations. Second, the stellar ra-
³⁶³ dius R_{\star} , mass M_{\star} , and other related parame-
³⁶⁴ ters are derived using empirical relations and
³⁶⁵ the above T_{eff} and [Fe/H] values.

³⁶⁶ 3.1.1. *Estimation of T_{eff} and [Fe/H]: from IRD ³⁶⁷ spectra*

³⁶⁸ We derived the effective temperature T_{eff} and
³⁶⁹ abundances of individual elements [X/H] from
³⁷⁰ the coadded IRD spectrum. To avoid ampli-
³⁷¹ fying noise in the spectrum, we decided not
³⁷² to deconvolve the instrumental profile prior to
³⁷³ these analyses.

³⁷⁴ We determined the parameters by the equiva-
³⁷⁵ luent width comparison of individual absorption
³⁷⁶ lines between the synthetic spectra and the ob-
³⁷⁷ served ones. For T_{eff} estimation, 47 FeH molec-
³⁷⁸ ular lines in the Wing-Ford band at 990 – 1020
³⁷⁹ nm was used as same as in Ishikawa et al.
³⁸⁰ (2022). We also derived the abundance of eight
³⁸¹ metal elements as described in Section A.1.

³⁸² We iterated the T_{eff} estimation and the abun-
³⁸³ dance analysis alternately until T_{eff} and metal-
³⁸⁴ licity were consistent with each other. First, we
³⁸⁵ derived a provisional T_{eff} assuming solar metal-
³⁸⁶ licity ([Fe/H] = 0), and then we determined
³⁸⁷ the individual abundances of the eight elements
³⁸⁸ [X/H] using this provisional T_{eff} . Second, we
³⁸⁹ redetermined T_{eff} adopting the iron abundance
³⁹⁰ [Fe/H] as the input metallicity, and then we re-
³⁹¹ determined the abundances using the new T_{eff} .
³⁹² We iterated the estimation of T_{eff} and [Fe/H]
³⁹³ until the final results and the results of the pre-
³⁹⁴ vious step agreed within the error margin. As
³⁹⁵ a result, we derived $T_{\text{eff}} = 3156 \pm 119$ K and
³⁹⁶ [Fe/H] = 0.333 ± 0.088 dex.

³⁹⁷ 3.1.2. *Estimation of T_{eff} and [Fe/H]: from SpeX ³⁹⁸ spectra and photometric relations*

³⁹⁹ Before analyzing our SpeX spectra, we cor-
⁴⁰⁰ rected the data to the lab reference frame

⁴⁰¹ using `tellrv`⁸ (Newton et al. 2014, 2022).
⁴⁰² We then determined metallicity with `metal`⁹
⁴⁰³ (Mann et al. 2013), using only the K-band part
⁴⁰⁴ of the spectrum, which is historically the most
⁴⁰⁵ reliable, although the metallicities from H- and
⁴⁰⁶ J-band are broadly consistent.

⁴⁰⁷ We calculated the stellar parameters using a
⁴⁰⁸ series of photometric relations, following the
⁴⁰⁹ Section 4.3 of (Dressing et al. 2019). First,
⁴¹⁰ we calculated the luminosity of the star us-
⁴¹¹ ing the Gaia EDR3 distance (Stassun & Torres
⁴¹² 2021), 2MASS J magnitude, r magnitude (from
⁴¹³ the Carlsberg Meridian Catalogue; Muñoz &
⁴¹⁴ Evans 2014), and the metallicity-dependent r-J
⁴¹⁵ bolometric correction in Table 3 of Mann et al.
⁴¹⁶ (2015). Next, we calculated the radius of the
⁴¹⁷ star using the relation between R_{\star} , absolute
⁴¹⁸ K magnitude, and [Fe/H] defined in Table 1
⁴¹⁹ of Mann et al. (2015). Lastly, we calculated
⁴²⁰ T_{eff} using the Stefan-Boltzmann law. As a re-
⁴²¹ sult, we derived $T_{\text{eff}} = 3207 \pm 99$ K and [Fe/H]
⁴²² = 0.338 ± 0.083 dex.

⁴²³ The strong agreement in T_{eff} and [Fe/H] be-
⁴²⁴ tween the two methods suggests a high degree
⁴²⁵ of reliability of the measurements. For the fol-
⁴²⁶ lowing analyses, we used the weighted mean of
⁴²⁷ the two respective measurements for T_{eff} and
⁴²⁸ [Fe/H], specifically, $T_{\text{eff}} = 3185 \pm 76$ K and
⁴²⁹ [Fe/H] = 0.336 ± 0.060 dex.

⁴³⁰ 3.1.3. *Estimation of stellar radius and mass*

⁴³¹ We estimated other stellar parameters such
⁴³² as stellar mass M_{\star} , radius R_{\star} , surface gravity
⁴³³ $\log g$, mean density ρ_{\star} , and luminosity L_{\star} fol-
⁴³⁴ lowing the procedure described in Hirano et al.
⁴³⁵ (2021). In short, the distributions of the stellar
⁴³⁶ parameters are derived from a Monte Carlo ap-
⁴³⁷ proach using a combination of several empirical
⁴³⁸ relations as well as the observed and literature
⁴³⁹ values.

⁴⁴⁰ The R_{\star} value was calculated through the em-
⁴⁴¹ pirical relation from Mann et al. (2015), and
⁴⁴² M_{\star} from Mann et al. (2019). In deriving the
⁴⁴³ stellar parameters by Monte Carlo simulations,
⁴⁴⁴ we adopted Gaussian distributions for T_{eff} and
⁴⁴⁵ [Fe/H] based on our spectroscopic analyses (see
⁴⁴⁶ Sections 3.1.1 and 3.1.2), the apparent K_s -
⁴⁴⁷ band magnitude from 2MASS, and the parallax
⁴⁴⁸ from Gaia EDR3 (Stassun & Torres 2021). We

⁸ <https://github.com/ernewton/tellrv>

⁹ <https://github.com/awmann/metal>

Table 1. Main identifiers, equatorial coordinates, proper motion, parallax, optical and infrared magnitudes, and fundamental parameters of TOI-1696.

Parameter	Value	Source
<i>Main identifiers</i>		
TIC	470381900	TIC v8 ^a
2MASS	J04210733+4849116	ExoFOP ^a
WISE	J042107.34+484911.5	ExoFOP ^a
UCAC4	695-028795	ExoFOP ^a
<i>Gaia EDR3</i>	270260649602149760	<i>Gaia EDR3</i> ^b
<i>Equatorial coordinates, parallax, and proper motion</i>		
R.A. (J2015.5)	04 ^h 21 ^m 07.36 ^s	<i>Gaia EDR3</i> ^b
Dec. (J2015.5)	+48°49'11.38"	<i>Gaia EDR3</i> ^b
π (mas)	15.4752 ± 0.0345	<i>Gaia EDR3</i> ^b
μ_α (mas yr ⁻¹)	12.8726 ± 0.0345	<i>Gaia EDR3</i> ^b
μ_δ (mas yr ⁻¹)	-19.0463 ± 0.0269	<i>Gaia EDR3</i> ^b
<i>Optical and near-infrared photometry</i>		
<i>TESS</i>	13.9664 ± 0.00730068	TIC v8 ^a
<i>G</i>	15.3056 ± 0.0028	<i>Gaia EDR3</i> ^b
<i>B_p</i>	17.0511 ± 0.0051	<i>Gaia EDR3</i> ^b
<i>R_p</i>	14.0457 ± 0.0039	<i>Gaia EDR3</i> ^b
<i>B</i>	18.467 ± 0.162	ExoFOP ^a
<i>V</i>	16.82 ± 1.133	ExoFOP ^a
<i>J</i>	12.233 ± 0.023	2MASS ^c
<i>H</i>	11.604 ± 0.031	2MASS ^c
<i>K_s</i>	11.331 ± 0.023	2MASS ^c
<i>W1</i>	11.134 ± 0.023	All WISE ^d
<i>W2</i>	10.984 ± 0.021	All WISE ^d
<i>W3</i>	10.71 ± 0.11	All WISE ^d
<i>W4</i>	8.748±	All WISE ^d
<i>Fundamental parameters</i>		
<i>T_{eff}</i> (K)	3185 ± 76	This work
log <i>g</i> (cgs)	4.959 ± 0.026	This work
[Fe/H] (dex)	0.336 ± 0.060	This work
<i>M_*</i> (<i>M_⊕</i>)	0.255 ± 0.0066	This work
<i>R_*</i> (<i>R_⊕</i>)	0.2775 ± 0.0080	This work
ρ_* (g cm ⁻³)	16.8 ^{+1.5} _{-1.4}	This work
distance (pc)	65.03 ± 0.36	This work
Luminosity (<i>L_⊕</i>)	0.00711 ^{+0.00083} _{-0.00075}	This work

^a<https://exofop.ipac.caltech.edu/tess/>

^bStassun & Torres (2021)

^cSkrutskie et al. (2006)

^dCutri et al. (2021)

assumed zero extinction ($A_V = 0$), considering the proximity of the star to Earth.

As a result, we derived $R_* = 0.2775 \pm 0.0080 R_{\odot}$ and $M_* = 0.255 \pm 0.0066 M_{\odot}$ along with the other parameters listed in A.1. By interpolating Table 5 of Pecaut & Mamajek (2013) we determined the spectral type of TOI-1696 to be M4V ($M3.9V \pm 0.2$).

To check the robustness of this analysis, we confirmed them to be in good agreement with stellar parameters derived through independent analyses based on SED fitting and ISOCHRONES (see Section A.2 and A.3).

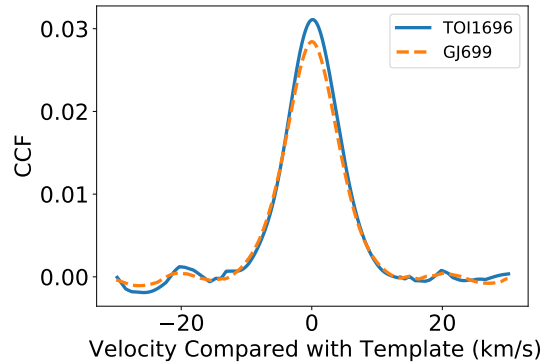


Figure 5. Calculated CCF of the IRD spectrum of TOI-1696 taken on 2021 January 30 at the orbital phase 0.247, to the template spectrum of GJ699, exhibiting a single peak with width 9.2 km s⁻¹. The dashed line shows the auto-correlation function of the GJ699 spectrum as a reference.

3.2. Search for spectroscopic binary stars

If a stellar companion orbits the target star, the observed spectra will generally be the combination of two stellar spectra with different radial velocities. To see if TOI-1696 is a spectroscopic binary (i.e. an SB2), we calculated the cross-correlation function (CCF) of the TOI-1696's IRD spectra with that of the well-known single-star GJ 699 (Barnard's Star). The spectrum of TOI-1696 used for the analysis was obtained on UT 2021 January 30 08:53, which corresponds to an orbital phase of 0.247 based on the *TESS* ephemeris.

For the analysis, we divided the spectra into six wavelength bins that are less affected by telluric absorption: [988, 993 nm], [995, 1000 nm], [1009, 1014 nm], [1016, 1021 nm], [1023, 1028 nm], and [1030, 1033 nm]. We corrected the telluric absorption signal using the spectra of the rapid-rotator HIP 74625, which was observed at the same night. The CCF to the template spectrum was calculated for each segment, after barycentric velocity correction. Finally, we computed the median of the CCFs from each segment. As shown in Figure 5, the resulting CCF is clearly single-peaked. If the observed transit signals were actually caused by an eclipsing stellar companion, the RV difference at quadrature would be > 100 km s⁻¹, which would result in a second peak in the CCF given that the flux of such a companion would be detectable. We thus conclude TOI-1696 is not an eclipsing binary.

495 **3.3. Stellar age**

496 Because young stars are active and rapidly ro-
 497 tating, stellar activity and rotation period can
 498 be used as proxy for determining its youth. We
 499 did not find any stellar rotational signal in the
 500 *TESS* SPOC light curve, suggesting that the
 501 star is not very active. Similarly, no strong
 502 rotational signal was found in archival photo-
 503 metric data from ZTF Data Release 9 (Bellm
 504 et al. 2019; Masci et al. 2019) and ASAS-SN
 505 (Kochanek et al. 2017).

506 GJ 699 has a rotation period of 145 days and
 507 $v \sin i$ of less than 3 km s^{-1} (Toledo-Padrón
 508 et al. 2019), which is below the limit of IRD’s
 509 resolving power (~ 70000 , corresponding to \sim
 510 4.5 km s^{-1}). While the CCF of TOI-1696 has
 511 a FWHM value consistent with that of GJ 699
 512 (see Figure 5), even if we assume the rotation
 513 axis of TOI-1696 is in the plane of the sky, rel-
 514 atively short rotation periods cannot be ruled
 515 out, as their rotational broadening would not
 516 be resolvable with IRD. However, fast rotation
 517 would most likely be accompanied with surface
 518 magnetic activity levels that would produce de-
 519 tectable photometric signals.

520 We also used `banyan` Σ (Gagné et al. 2018)
 521 to check if TOI-1696 is a member of any known
 522 stellar associations, using its proper motion
 523 and the parallax from *Gaia* EDR3. `banyan` Σ
 524 tool¹⁰ returned a value of 99.9% field star, sug-
 525 gesting it is not a member of any nearby young
 526 moving group. The non-detection by GALEX
 527 also means that the star is not young enough
 528 to be bright in the UV. We thus conclude that
 529 TOI-1696 is most likely a relatively old, slow
 530 rotator.

531 **3.4. Transit analysis**

532 We jointly fit the *TESS*, KeplerCam, Sin-
 533 istro, MuSCAT3, and MuSCAT datasets using
 534 the PyMC3 (Salvatier et al. 2016), exoplanet¹¹
 535 (Foreman-Mackey et al. 2019), starry (Luger
 536 et al. 2019), and celerite2 (Foreman-Mackey
 537 et al. 2017; Foreman-Mackey 2018) software
 538 packages. The model assumes a chromatic
 539 transit depth, a linear ephemeris, a circular or-
 540 bit, and quadratic limb darkening. For efficient
 541 and uninformative sampling, the quadratic
 542 limb darkening coefficients were transformed

543 following Kipping (2013). To account for sys-
 544 tematics in the ground-based datasets we in-
 545 cluded a linear model of airmass and other co-
 546 variates, such as the pixel response function
 547 peak, width, and centroids, when available. To
 548 account for stellar variability and residual sys-
 549 tematics in the *TESS* SPOC light curve, we in-
 550 cluded a Gaussian Process (GP Rasmussen &
 551 Williams 2005) model with a Matérn-3/2 co-
 552 variance function. To account for the possibil-
 553 ity of under- or over-estimated uncertainties,
 554 we included a white noise scale parameter for
 555 each dataset/band, enabling the errors to be
 556 estimated simultaneously with other free pa-
 557 rameters; we placed Gaussian priors on these
 558 white noise scale parameters, with center and
 559 width equal to unity. We placed Gaussian pri-
 560 ors on the stellar mass and radius based on the
 561 results in Table 1. We also placed Gaussian
 562 priors on the limb darkening coefficients based
 563 on interpolation of the parameters tabulated in
 564 Claret et al. (2012) and Claret (2017), propa-
 565 gating the uncertainties in the stellar param-
 566 eters in Table 1 via Monte Carlo simulation.

567 To optimize the model we used the gradient-
 568 based BFGS algorithm (Nocedal & Wright 2006)
 569 implemented in `scipy.optimize` to find initial
 570 maximum a posteriori (MAP) parameter esti-
 571 mates. We then used these estimates to initial-
 572 ize an exploration of parameter space via “no
 573 U-turn sampling” (NUTS, Hoffman & Gelman
 574 2014), an efficient gradient-based Hamiltonian
 575 Monte Carlo (HMC) sampler implemented in
 576 PyMC3.

577 Detailed plots showing the model fits to the
 578 ground-based datasets are shown in Figure 7,
 579 Figure 8, and Figure 9. We did not detect
 580 any significant wavelength dependence of the
 581 transit depth (see Figure 10), which rules out
 582 many plausible false positive scenarios involv-
 583 ing eclipsing binaries (see Section 3.6 for more
 584 details). The results of this fit are listed in
 585 Table 2. Having established the achromaticity
 586 of the transit depth, we conducted a second fit
 587 with an achromatic model to robustly estimate
 588 the planet radius. This fit resulted in a final
 589 value of $R_P/R_\star = 0.1025 \pm 0.0014$, correspond-
 590 ing to an absolute radius of $3.09 \pm 0.11 R_\oplus$, and
 591 all other parameters were unchanged.

592 **3.5. Companion mass constraints**

593 To put a limit on the mass of TOI-1696.01, we
 594 fit an RV model with a circular orbit to the RV

¹⁰ <http://www.exoplanetes.umontreal.ca/banyan/>

¹¹ <https://docs.exoplanet.codes/en/stable/>

Table 2. Results of joint fit to the *TESS* and ground-based transit datasets.

Parameter	Value
<i>Primary transit parameters</i>	
M_* [M_\odot]	0.255 ± 0.007
R_* [R_\odot]	0.277 ± 0.008
T_0 [BJD]	$2458834.20115 \pm 0.000058$
P [days]	2.500311 ± 0.000004
$R_P/R_{*,T}$	0.0952 ± 0.0062
$R_P/R_{*,V}$	0.1021 ± 0.0057
$R_P/R_{*,g}$	$0.1036^{+0.0060}_{-0.0068}$
$R_P/R_{*,r}$	0.1053 ± 0.0034
$R_P/R_{*,i}$	0.1023 ± 0.0020
$R_P/R_{*,z}$	0.1026 ± 0.0020
R_P/R_*	0.1025 ± 0.0014^a
b	$0.59^{+0.03}_{-0.04}$
<i>Limb darkening parameters</i>	
$u_1(T)$	0.16 ± 0.01
$u_2(T)$	0.48 ± 0.01
$u_1(V)$	0.48 ± 0.02
$u_2(V)$	0.30 ± 0.01
$u_1(g)$	0.49 ± 0.01
$u_2(g)$	0.31 ± 0.01
$u_1(r)$	0.50 ± 0.01
$u_2(r)$	0.25 ± 0.01
$u_1(i)$	0.37 ± 0.01
$u_2(i)$	0.28 ± 0.01
$u_1(z)$	0.24 ± 0.01
$u_2(z)$	0.36 ± 0.01
<i>Derived parameters</i>	
R_p [R_\oplus]	3.09 ± 0.11^a
a [AU]	0.0229 ± 0.0002
T_{eq} [K]	489 ± 13^b
T_{14} [hours]	1.00 ± 0.01

^aDerived from achromatic transit model fit.

^bAssuming a Bond albedo of 0.3.

595 data from Subaru/IRD. Between the H -band
596 and the YJ -band spectra obtained with IRD,
597 we opted to use the H -band spectra for RV
598 analysis because of its higher SNR.¹² The data
599 observed on 2021 January 29 was excluded be-

¹² There have been reports of unpredictable systematic errors caused by persistence light on the detector in H -band, especially when bright stars are observed before fainter stars. We checked the objects observed before TOI-1696 and found that none were more than 1.2 mag brighter in the H -band, i.e. persistence light isn't likely to be a problem with these data.

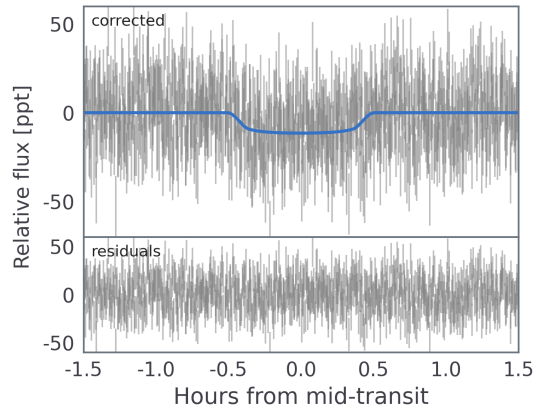


Figure 6. The phase-folded *TESS* light curve after removing the best-fit GP noise model, with the best-fit transit model (blue) from our joint analysis of the *TESS* and ground-based light curves.

600 cause of the possibility of an RV offset, as there
601 was a gap of 8 months relative to the succeed-
602 ing observations. We also removed any data
603 with the clouds passing, which can cause sys-
604 tematic errors. The final dataset consisted of 9
605 RV measurements from 2021 September 29 to
606 2022 January 8.

607 We used the RV model included in PyTransit
608 which we simplified to have five free parame-
609 ters: phase-zero epoch T_0 , period, RV semi-
610 amplitude, RV zero point, and RV jitter term.
611 For the T_0 and the period, we put Gaussian
612 priors using the T_0 and period derived from the
613 transit analysis. For the other parameters we
614 put wide uniform priors. We ran the built-in
615 Differential Evolution optimizer and then sam-
616 ple the parameters with Markov Chain Monte
617 Carlo (MCMC) using 30 walkers and 10^4 steps.
618 We use the following equation to derive the
619 planet mass,

$$620 M_p = \left(\frac{PM_s^2}{2\pi} \right)^{1/3} \frac{K(1-e^2)^{1/2}}{\sin(i)} \quad (1)$$

621 where M_p is planet mass, M_* is star mass, P
622 is orbital period, K is RV semi-amplitude, e is
623 eccentricity (fixed to zero), and i is inclination
624 (fixed to 90°). To propagate uncertainties, we
625 use the posteriors for M_* and P from previous
626 analyses.

627 In Figure 11 we plot Keplerian orbital mod-
628 els corresponding to different masses encom-
629 passing the 68th, 95th, and 99.7th percentiles of
630 the semi-amplitude posterior distribution. The
631 2- σ upper limit is $48.8 M_\oplus$ which places the
632 companion 2 orders of magnitude below the

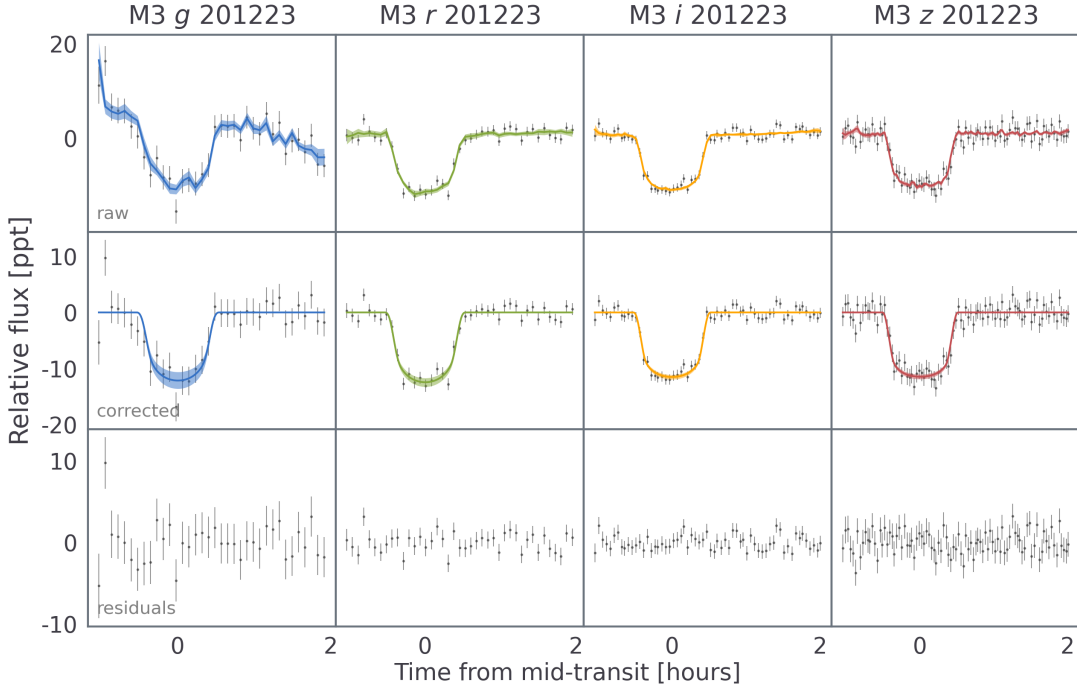


Figure 7. Transit model fit to the MuSCAT3 (M3) data from 2020 December 23, ordered column-wise per bandpass. The top row shows the raw data with the transit and systematics model, the middle row shows the systematics-corrected data with only the transit model, and the bottom row shows the residuals from the fit. The colors of the model correspond to the photometric bandpass of each dataset; see also Figure 10.

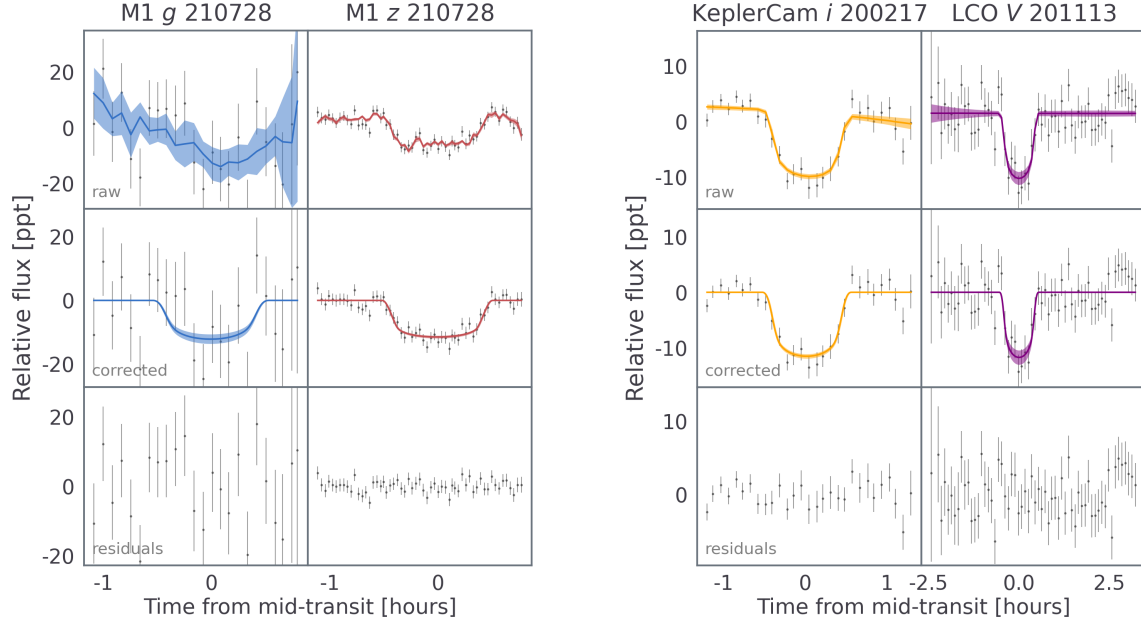


Figure 8. Same as Figure 7, but for the MuSCAT (M1) data from 2021 July 28.

633 deuterium burning mass limit. The best-fit
 634 semi-amplitude is $K = 14.4 \text{ ms}^{-1}$, which cor-
 635 responds to a mass of $M_p = 12.3 M_\oplus$, and the
 636 best-fit jitter value is $\sigma_K = 62 \text{ ms}^{-1}$.

Figure 9. Same as Figure 7, but for the Kepler-
 Cam *i* 200217 and LCO *V* 201113

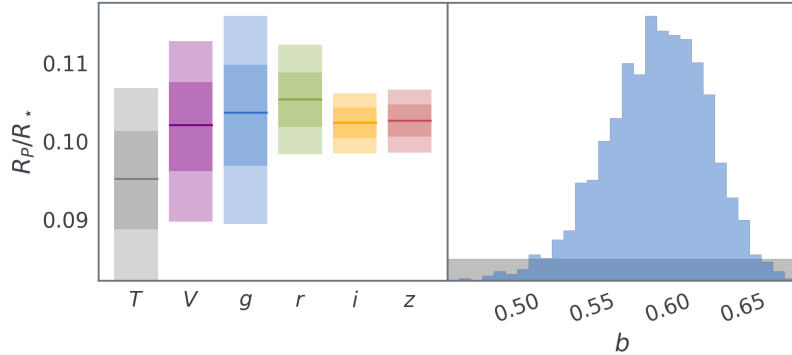


Figure 10. Posteriors of the planet-to-star radius ratio (R_p/R_*) in each bandpass (left) and impact parameter (right) from the joint fit to the *TESS* data and the ground-based data shown in Figure 7, Figure 8, and Figure 9; the gray shaded region in the right panel represents the uniform prior used in the fit, while the blue histogram is the posterior.

We calculated an expected planetary mass of $\sim 8 M_{\oplus}$ with MRExo¹³, which uses a mass-radius relationship calibrated for planets around M dwarfs (Kanodia et al. 2019). This mass corresponds to a semi-amplitude of 9.4 m s^{-1} , but the observed RV data exhibits significantly larger variability ($\sigma \approx 52 \text{ m s}^{-1}$). We interpret this variability as being responsible for the large jitter value found by the fit, which suggests it is out-of-phase with TOI-1696.01. Since the star appears to be quiet, one explanation for this signal is the existence of an additional (possibly non-transiting) planet, but more RV measurements would be required to determine if this is the case. Furthermore, if such a planet were dynamically interacting with TOI-1696.01, then this could help explain TOI-1696.01’s location in a sparsely populated part of the period-radius plane (see Section 4).

3.6. Eliminating false positive scenarios

A number of astrophysical scenarios can mimic the transit signal detected from *TESS* photometry, including an eclipsing binary (EB) with a grazing transit geometry, a hierarchical EB (HEB), and a diluted eclipse of a background (or foreground) EB (BEB) along the line of sight of the target. In the following, we will examine the plausibility of each scenario. First, the Renormalised Unit Weight Error (RUWE) from *Gaia* EDR3 is 1.12, which suggests that TOI-1696 is single (Belokurov et al. 2020). We can also rule out the EB scenario based on the analysis of the IRD CCF in Section 3.2, and the mass constraint derived in

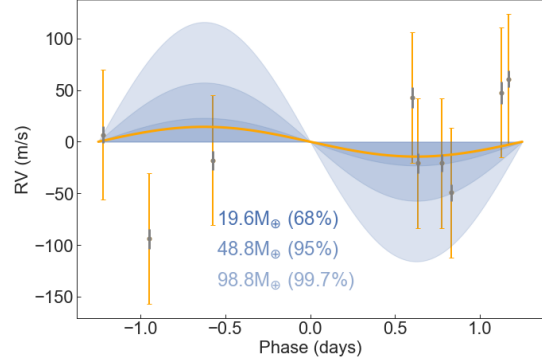


Figure 11. Phase-folded RVs with Keplerian models corresponding to the 1-, 2-, and 3- σ mass upper limits. Gray points with the error bars show the errors estimated from the data processing method described in Section 2.8. The error bars in orange show the original errors + jitter term value of 62 m s^{-1} (added in quadrature) from the best-fit RV model (orange line, best $M_p = 12.3 M_{\oplus}$.)

Section 3.1.1. Finally, the absence of any wavelength dependence of the transit depth from our chromatic transit analysis (Section 3.4) is incompatible with contamination from a star of different spectral type (colour) than the host star, the details of which are discussed in the Appendix B. In the absence of dilution, the measured radius of $3.09 \pm 0.11 R_{\oplus}$ ($0.27 R_{Jup}$) equals the true radius, which makes it significantly smaller than the lower limit of $0.8 R_{Jup}$ expected for brown dwarfs (Burrows et al. 2011).

Grazing transit geometries can also be eliminated, as the impact parameter is constrained to $b < 0.7$ at the 99% level based on our transit and contamination analyses. The apparent boxy shape of our follow-up lightcurves is in

¹³ <https://github.com/shbhuk/mrexo>

688 stark contrast with the V-shaped transit ex-
 689 pected for grazing orbits. Hence, grazing EB
 690 scenario is ruled out.

691 Moreover, we can constrain the classes of
 692 HEBs that can reproduce the observed transit
 693 depth and shape using our multi-band obser-
 694 vations. We aim to compute the eclipse depths
 695 for a range of plausible HEBs in the bluest and
 696 reddest bandpasses where they are expected to
 697 vary significantly. We adopt the method pre-
 698 sented in Bouma et al. (2020) to perform the
 699 calculation taking into account non-zero im-
 700 pact parameter, the details of which are dis-
 701 cussed in the Appendix C. Comparing the sim-
 702 ulated eclipse depths with the observed depth
 703 in each band, we found that there is no plau-
 704 sible HEB configuration explored in our simu-
 705 lation that can reproduce the observed depths
 706 in multiple bands simultaneously. Hence, the
 707 HEB scenario is ruled out.

708 Although, TOI-1696’s probability of being a
 709 BEB is very high a priori given its location at
 710 the galactic plane, we argue in the following
 711 that the BEB scenario is extremely unlikely.
 712 Our MuSCAT3 observation can resolve the sig-
 713 nal down to $3''$, which represents the maxi-
 714 mum radius within which the signal must origi-
 715 nate. Furthermore, our high-resolution speckle
 716 imaging ruled any nearby star and blended
 717 sources down to $0.1''$ at a delta mag of 4.5.
 718 We checked archival images taken more than
 719 60 years apart, but the proper motion of TOI-
 720 1696 is not enough to obtain a clear view along
 721 the line of sight of the star. However, we can
 722 use statistical arguments to estimate the prob-
 723 ability of a chance-aligned star. To do this,
 724 we use the population synthesis code TRILE-
 725 GAL¹⁴ (Girardi et al. 2005), which can simu-
 726 late the Galactic stellar population along any
 727 line of sight. Given the position of TOI-1696,
 728 we found a probability of 5×10^{-8} to find
 729 a star brighter than $T=16^{15}$, within an area
 730 equal to the smallest MuSCAT3 photometric
 731 aperture (aperture radius = $3''$). Assuming
 732 all such stars are binary and preferentially ori-
 733 ented edge-on to produce eclipses with period
 734 and depth consistent with the *TESS* detection,

¹⁴ <http://stev.oapd.inaf.it/cgi-bin/trilegal>

¹⁵ T denotes the *TESS* bandpass. The maximum delta magnitude was computed using $dT = -2.5 \log_{10}(\text{depth})$, which translates to the magnitude that can produce a 100% eclipse

735 then this can represent a very conservative up-
 736 per limit of a BEB scenario. Despite the small
 737 probability of a BEB based on the trivial star
 738 counting argument, we discuss relevant tools
 739 in the following section for a more thorough
 740 statistical modeling.

741 3.7. Statistical validation

742 Here we quantify the false positive probabil-
 743 ity (FPP) of TOI-1696.01 using the Python
 744 package VESPA and TRICERATOPS (Morton
 745 2015; Giacalone & Dressing 2020), the details
 746 of which are discussed in Section D. Although
 747 we were able to rule out the classes of EB,
 748 BEB, and HEB in Section 3.6, we ran VESPA
 749 considering all these scenarios for completeness
 750 and computed a formal $\text{FPP} < 1 \times 10^{-6}$ which
 751 robustly quantifies TOI-1696.01 as a statisti-
 752 cally validated planet. Additionally, we val-
 753 idated TOI-1696.01 using TRICERATOPS and
 754 found $\text{FPP}=0.0020$. Giacalone et al. (2021)
 755 noted that TOIs with $\text{FPP} < 0.015$ have a high
 756 enough probability of being bona fide planets
 757 to be considered validated. The low FPPs cal-
 758 culated using VESPA and TRICERATOPS added
 759 further evidence to the planetary nature of
 760 TOI-1696.01. We now refer to the planet as
 761 TOI-1696 b in the remaining sections.

762 4. DISCUSSION

763 4.1. The nature of the planet

764 Here, we consider the nature of TOI-1696 b
 765 by placing it in context with the population of
 766 known exoplanets¹⁶. Figure 12 shows a radius
 767 vs period diagram, indicating that there are
 768 only a handful of planets with similar charac-
 769 teristics to TOI-1696 b. The measured plane-
 770 tary radius R_p of $3.09 \pm 0.11 R_\oplus$ and the orbital
 771 period P of 2.50031 ± 0.00001 days, places it
 772 securely within the bounds of the Neptunian
 773 desert as defined by Mazeh et al. (2016). The
 774 region occupied by TOI-1696 remains sparsely
 775 populated despite recent discoveries of *TESS*
 776 planets within the Neptunian desert (e.g. Mur-
 777 gas et al. 2021; Brande et al. 2022).

778 It should be noted that the Neptunian desert
 779 was originally determined based on a popula-
 780 tion of planets orbiting mainly solar-type stars

¹⁶ Based on a query of the NASA Exoplanet Archive “Confirmed Planets” table on 2022 January 31, <https://exoplanetarchive.ipac.caltech.edu/>

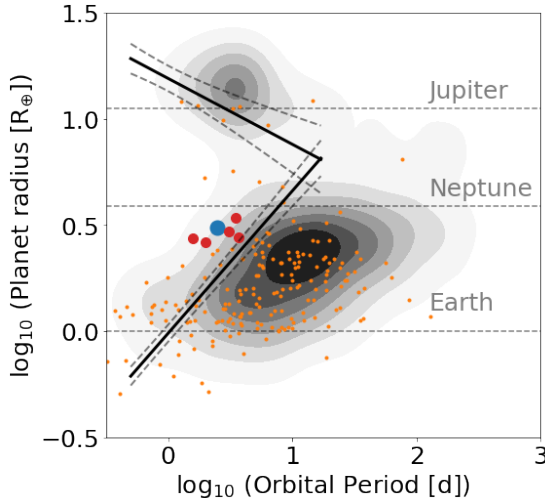


Figure 12. TOI-1696 b (blue) in the context of known transiting planets (contours). TOI-1696 b appears to be within or close to the boundaries of the Neptunian desert (solid black lines) in the period-radius plane defined by Mazeh et al. (2016). The dashed lines refer to the boundaries' uncertainty regions. The orange points indicate planets orbiting M dwarfs ($T_{\text{eff}} < 3800\text{K}$) and the red points indicate the five planets most similar in this parameter space to TOI-1696 b: K2-25 b, K2-320 b, GJ 1214 b, TOI-269 b, and TOI-2406 b.

from the *Kepler* mission. Because TOI-1696 is an M dwarf, the incident flux at a given orbital separation will be less than solar-type stars. Nevertheless, we emphasize that the target exists in a sparsely populated region of parameter space, despite the large number of planets discovered around M dwarfs since the *Kepler* mission (i.e. from *K2* and *TESS*). For example, if we limit the comparison to the 279 confirmed planets around M dwarfs with T_{eff} below 3800 K, only 14 planets have been found so far with orbital periods shorter than 10 days and planetary radii in the range $2.5R_{\oplus} < R_p < 5R_{\oplus}$. As shown in Figure 12, TOI-1696 b is similar to K2-25 b (Mann et al. 2016), K2-320 b (Castro González et al. 2020), GJ 1214 b (Charbonneau et al. 2009), TOI-269 b (Cointepas et al. 2021), and TOI-2406 b (Wells et al. 2021) in terms of orbital period and radius. In particular, TOI-2406 b appears most similar to TOI-1696 b as it orbits around a mid-M dwarf with an effective temperature of 3100 ± 75 , and has a radius of $2.94 \pm 0.17 R_{\oplus}$ and orbital period of 3.077 days. TOI-2406 is also thought to be relatively old without any activity signal. As both TOI-1696 b and TOI-2406 b are excellent targets for

detailed characterization studies, together they may provide unique insights into this class of planet. There is also some similarity between TOI-1696 b and the Neptunian Desert planets orbiting young host stars, such as AU Mic b and c, K2-25 b, K2-95 b and K2-264 b. It has been suggested that these planets may have inflated radii and could possibly still be undergoing atmospheric mass-loss (e.g. Mann et al. 2016). Further study of TOI-1696 b could reveal whether its similarity to these planets (despite being older) is only superficial, or if it is indicative of an inflated radius.

4.2. Prospects for transmission spectroscopy

Given the rarity of this planet, it would be useful to assess its prospects for future atmospheric observations to understand its formation and evolution. In particular, the relatively large size of the planet compared to its host star makes it a good candidate for transmission spectroscopy. Using Equation 1 in Kempton et al. (2018), we calculated the transmission spectroscopy metric (TSM) of TOI-1696 b from its mass, radius, equilibrium temperature, stellar radius, and J-band magnitude. We used the values in Figure 1 and 2, and assumed a mass of $8 M_{\oplus}$ estimated by MRExo. The derived TSM value of TOI-1696 b is 105.6. For reference, Kempton et al. (2018) suggested that planets with $\text{TSM} > 90$ are ideal targets for atmospheric follow-up.

For comparison, we calculated the TSM for the known population of transiting M dwarf planets. We selected planets with $T_{\text{eff}} < 3800\text{K}$, $R_p < 10R_{\oplus}$, and $H < 11\text{mag}$ ¹⁷. For planets without mass measurements, we assumed the masses predicted by MRExo. For planets without an equilibrium temperature, we estimated it from the semi-major axis and the host star's effective temperature (assuming zero albedo). Figure 13 shows the computed TSM values for the selected samples of planets. The TSM of TOI-1696 b places it in the top 10, making it one of the best targets for future atmospheric investigations.

4.3. Existence of a primordial atmosphere

Up to this point in the section, the discussion has been based on the assumption that

¹⁷ Based on a query of the NASA Exoplanet Archive Confirmed Planets table as of 2022 January 31

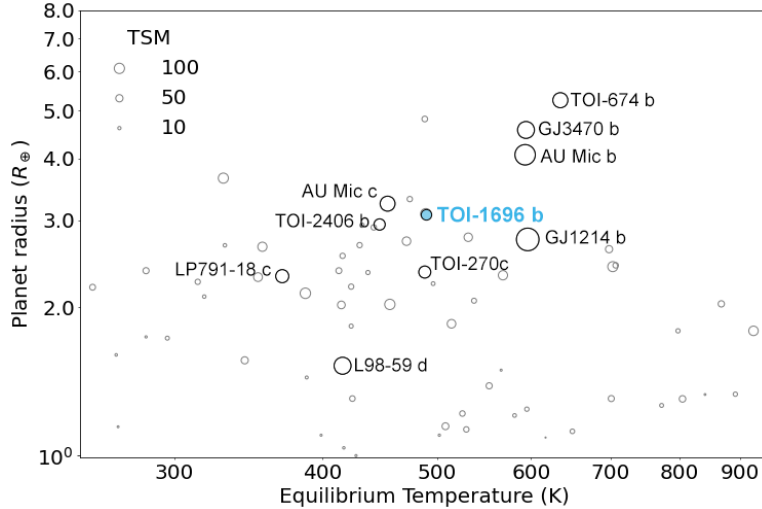


Figure 13. Planetary equilibrium temperature vs radius for TOI-1696 b and other planets with $R_p < 10R_\oplus$, with the host stars having $T_{\text{eff}} < 3800\text{K}$ and $H < 11\text{mag}$. The point size represents the calculated TSM values. Data points with a planet name beside them are those with a higher TSM values than the target.

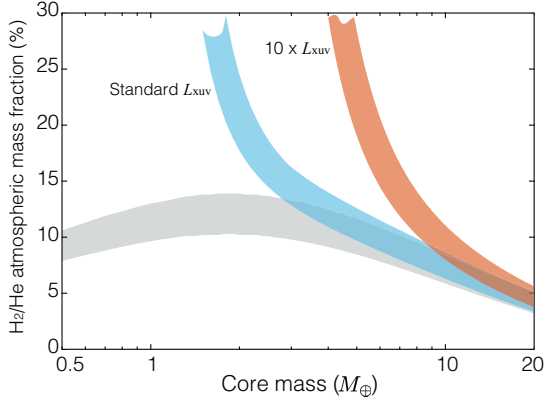


Figure 14. Initial H_2/He atmospheric mass fraction of a TOI-1696 b-like planet that satisfies the radius of $3.09 \pm 0.11 R_\oplus$ and $T_{\text{eq}} = 489 \pm 13\text{K}$ after photo-evaporative mass loss for 8 Gyr under the standard XUV radiation field (L_{XUV}) and $10L_{\text{XUV}}$. The grey region shows the H_2/He atmospheric mass fraction that reproduces the observed radius of TOI-1696 b with a rocky core.

the target has an atmosphere. Usually it is thought that planets above the so-called radius gap can retain their atmospheres (Weiss & Marcy 2014; Rogers 2015). However, does TOI-1696 b actually have an H_2/He atmosphere? Here we study the atmospheric mass that TOI-1696 b can retain after $\sim 8\text{Gyr}$ under a stellar XUV irradiation. The mass of TOI-1696 b remains poorly constrained as discussed in Section 3.5. We modeled TOI-1696 b as a rocky planet with Earth-like core compositions ($\text{MgSiO}_3:\text{Fe} = 7:3$) in the mass range from $0.5M_\oplus$ to $20M_\oplus$. The silicate man-

tle and iron core were described by the 3rd-order Birch-Murnaghan EoS for MgSiO_3 perovskite (Karki et al. 2000; Seager et al. 2007) and the Vinet EoS for ϵ -Fe (Anderson et al. 2001), respectively. The Thomas-Fermi Dirac EoS (Salpeter & Zapsolsky 1967) was applied to high-pressure EoS for MgSiO_3 at $P \geq 4.90\text{TPa}$ and Fe at $P \geq 2.09 \times 10^4\text{GPa}$ (Seager et al. 2007; Zeng & Sasselov 2013). The pressure and temperature in a H_2/He envelope were calculated using the SCvH EoS (Saumon et al. 1995).

We computed the thermal evolution of TOI-1696 b with a H_2/He atmosphere by calculating its interior structure in hydrostatic equilibrium for $\sim 8\text{Gyr}$, and calculated its mass loss process. The initial mass fraction of a H_2/He atmosphere for a rocky planet ranges from 0.001% to 30% of its core mass. The energy-limited hydrodynamic escape (Watson et al. 1981) controls the mass loss rate given by

$$\frac{dM_p}{dt} = -\eta \frac{R_p^3 L_{\text{XUV}}(t)}{4GM_p a^2 K_{\text{tide}}}, \quad (2)$$

η is the heating efficiency due to stellar XUV irradiation, L_{XUV} is the stellar XUV luminosity, G is the gravitational constant, and R_p is the planetary radius (Erkaev et al. 2007). Since the heating efficiency for a hydrogen-rich upper atmosphere was lower than 20% (Shematovich et al. 2014; Ionov & Shematovich 2015), we adopted $\eta = 0.1$. K_{tide} is the reduction factor of a gravitational potential owing to the

effect of a stellar tide:

$$K_{\text{tide}}(\xi) = 1 - \frac{3}{2\xi} + \frac{1}{2\xi^3} < 1, \quad \xi = \frac{R_H}{R_p}, \quad (3)$$

where R_H is the Hill radius. The XUV luminosity (L_{XUV}) of TOI-1696 followed from the X-ray-to-bolometric luminosity relations of M-type stars (Jackson et al. 2012), where we adopted the current luminosity of TOI-1696 as its bolometric luminosity. We also considered a $10L_{\text{XUV}}$ model because of the large uncertainty in L_{XUV} of young M dwarfs.

Figure 14 shows the initial H₂/He atmosphere of a TOI-1696 b-like planet that reproduces the radius of $3.09 \pm 0.11 R_\oplus$ at the current location (i.e., $T_{\text{eq}} = 489 \pm 13$ K) after the mass loss driven by the standard XUV radiation (L_{XUV} : blue) and 10 times higher one ($10L_{\text{XUV}}$: red). The grey region shows the H₂/He atmospheric mass fraction of TOI-1696 b with a rocky core that satisfies its observed radius. The observed radius of TOI-1696 b favors the existence of a H₂/He atmosphere atmosphere with $\gtrsim 3$ wt% unless its core contains icy material. We find that TOI-1696 b can possess the H₂/He atmosphere for 8 Gyr if its core mass is larger than $\sim 1.5 M_\oplus$ ($\sim 4 M_\oplus$ for $10L_{\text{XUV}}$ models). If TOI-1696 b initially had the H₂/He atmosphere of $\lesssim 3\%$, it should be completely lost. Also, TOI-1696 b with mass of $\gtrsim 10 M_\oplus$ can retain almost all the H₂/He atmosphere accreted from a disk. These suggest that TOI-1696 b with a rocky core of $\gtrsim 1.5 - 4 M_\oplus$ is likely to be a sub-Neptune with a H₂/He atmosphere.

5. CONCLUSIONS

TESS found transit signals of a sub-Neptune planet orbiting a mid-M dwarf TOI-1696. To validate and characterize the planetary system, we conducted follow-up observations of this system including ground-based transit photometry, high-resolution imaging, and high- and medium-resolution spectroscopy.

We have used several methods to determine the stellar parameters based on the results of the spectroscopic observations, and have confirmed that the results are consistent. The host star, TOI-1696, is a M-type star with a M_\star at $0.255 \pm 0.0066 M_\odot$ and T_{eff} at 3185 ± 76 K.

The fact that this target is located near the Galactic plane makes validation difficult. We used the results obtained to rule out various scenarios that could reproduce the *TESS* signal (grazing EB, HEB, and BEB).

The validated planet, TOI-1696 b is a Sub-Neptune size planet with the radius at $3.09 R_\oplus$ and rotation period at 2.5 days, which locates in the Neptunian desert. To see its atmospheric properties, we calculated how much of the atmosphere it currently retains, and found the planet likely to retain the H₂/He atmosphere if it has a core of $> 1.5 - 4 M_\oplus$. In order to statistically evaluate the feasibility of transmission spectroscopy on this planet, we have also calculated and compared the TSM and concluded that this target is one of the planets with the best prospects for atmospheric detection among the currently known Sub-Neptune-sized planets. In addition, future RV observations with high-resolution infrared spectrographs such as IRD will allow us to place more substantial limits on the planetary mass.

6. ACKNOWLEDGEMENTS

Funding for the *TESS* mission is provided by NASA's Science Mission Directorate. We acknowledge the use of public *TESS* data from pipelines at the *TESS* Science Office and at the *TESS* Science Processing Operations Center. This research has made use of the Exoplanet Follow-up Observation Program website, which is operated by the California Institute of Technology, under contract with the National Aeronautics and Space Administration under the Exoplanet Exploration Program. Resources supporting this work were provided by the NASA High-End Computing (HEC) Program through the NASA Advanced Supercomputing (NAS) Division at Ames Research Center for the production of the SPOC data products. This paper includes data collected by the *TESS* mission that are publicly available from the Mikulski Archive for Space Telescopes (MAST).

This work makes use of observations from the Las Cumbres Observatory global telescope network. Some of the observations in the paper is based on observations made with the MuSCAT3 instrument, developed by Astrobiology Center and under financial supports by JSPS KAKENHI (JP18H05439) and JST PRESTO (JPMJPR1775), at Faulkes Telescope North on Maui, HI, operated by the Las Cumbres Observatory.

This research is in part on data collected at the Subaru Telescope, which is operated by the National Astronomical Observatory of

Japan, and at the Gemini North telescope, located within the Maunakea Science Reserve and adjacent to the summit of Maunakea. We are honored and grateful for the opportunity of observing the Universe from Maunakea, which has cultural, historical, and natural significance in Hawaii. Our data reductions benefited from PyRAF and PyFITS that are the products of the Space Telescope Science Institute, which is operated by AURA for NASA. This research made use of Astropy,¹⁸ a community-developed core Python package for Astronomy (Astropy Collaboration et al. 2013, 2016 2018). Some of the observations in the paper made use of the High-Resolution Imaging instrument(s) ‘Alopeke.’ Alopeke was funded by the NASA Exoplanet Exploration Program and built at the NASA Ames Research Center by Steve B. Howell, Nic Scott, Elliott P. Horch, and Emmett Quigley. ‘Alopeke (and/or Zorro) was mounted on the Gemini North (and/or South) telescope of the international Gemini Observatory, a program of NSF’s NOIRLab, which is managed by the Association of Universities for Research in Astronomy (AURA) under a cooperative agreement with the National Science Foundation. on behalf of the Gemini partnership: the National Science Foundation (United States), National Research Council (Canada), Agencia Nacional de Investigación y Desarrollo (Chile), Ministerio de Ciencia, Tecnología e Innovación (Argentina), Ministério da Ciência, Tecnologia, Inovações e Comunicações (Brazil), and Korea Astron-

omy and Space Science Institute (Republic of Korea). Some of the observations in this paper made use of the Infrared Telescope Facility, which is operated by the University of Hawaii under contract 80HQTR19D0030 with the National Aeronautics and Space Administration. The IRTF observations were collected under the program 2020B115 (PI: S. Giacalone). This work has made use of data from the European Space Agency (ESA) mission *Gaia* (<https://www.cosmos.esa.int/gaia>), processed by the *Gaia* Data Processing and Analysis Consortium (DPAC, <https://www.cosmos.esa.int/web/gaia/dpac/consortium>). Funding for the DPAC has been provided by national institutions, in particular the institutions participating in the *Gaia* Multilateral Agreement. This work is supported by Grant-in-Aid for JSPS Fellows, Grant Number JP20J21872, JSPS KAKENHI Grant Numbers JP20K14518, JP19K14783, JP21H00035, JP18H05439, JP18H05439, JP20K14521, JP17H04574, JP21K20376, JP21K13975, JP18H05442, JP15H02063, and JP22000005, SATELLITE Research from Astrobiology Center (Grant Number AB031010, AB022006, and AB031014), and JST CREST Grant Number JPMJCR1761.

E. E-B. acknowledges financial support from the European Union and the State Agency of Investigation of the Spanish Ministry of Science and Innovation (MICINN) under the grant PRE2020-093107 of the Pre-Doc Program for the Training of Doctors (FPI-SO) through FSE funds.

1072

APPENDIX

1073 A. DETAILED METHODS OF STELLAR
1074 PARAMETER ESTIMATION
1075 A.1. *Abundances of eight metal elements*
1076 *from IRD spectra*

1077 We calculated the abundances of seven other
1078 elements other than iron from IRD spectra.
1079 We used 28 lines in total caused by neutral
1080 atoms of Na, Mg, Ca, Ti, Cr, Mn, and Fe
1081 and singly ionized Sr. The detailed procedures
1082 of abundance analysis and error estimation are
1083 described in Ishikawa et al. (2020). Figure A.15

1084 shows the final values of abundance after the
1085 iteration. From the final values of the abundances of the eight elements, [M/H] was determined by calculating the average weighted by the inverse of the square of their estimated errors.

1090 A.2. *Estimation of Stellar Radius and Mass:*
1091 *SED Fitting*

1092 As an independent determination of the basic stellar parameters, we performed an analysis of the broadband spectral energy distribution (SED) of the star together with the *Gaia* EDR3 parallax (Stassun & Torres 2021), in order to determine an empirical measurement of

¹⁸ <http://www.astropy.org>

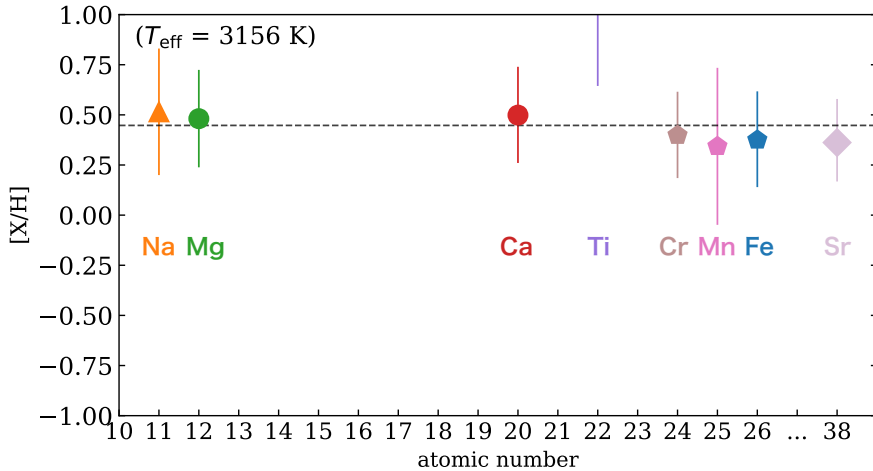


Figure A.15. Metallicity values derived from IRD spectrum. The horizontal dashed line corresponds to the weighted average $[M/H]$.

the stellar radius, following the procedures described in Stassun & Torres (2016); Stassun et al. (2017, 2018). We pulled the JHK_S magnitudes from 2MASS, the W1–W3 magnitudes from WISE, and the *grizy* magnitudes from Pan-STARRS. Together, the available photometry spans the full stellar SED over the wavelength range 0.4–10 μm (see Figure A.16).

We performed a fit using NExtGen stellar atmosphere models, with the effective temperature (T_{eff}) and metallicity ($[\text{Fe}/\text{H}]$) constrained from the spectroscopic analysis. The remaining free parameter is the extinction A_V , which we fixed at zero due to the star’s proximity. The resulting fit (Figure A.16) has a reduced χ^2 of 1.7. Integrating the (unreddened) model SED gives the bolometric flux at Earth, $F_{\text{bol}} = 5.20 \pm 0.25 \times 10^{-11} \text{ erg s}^{-1} \text{ cm}^{-2}$. Taking the F_{bol} and T_{eff} together with the *Gaia* parallax, gives the stellar radius, $R_\star = 0.276 \pm 0.015 R_\odot$. We used the T_{eff} and $[\text{Fe}/\text{H}]$ values from spectroscopic results as priors for the parameter estimation.

In addition, we estimated the stellar mass from the empirical relations of Mann et al. (2019), giving $M_\star = 0.279 \pm 0.014 M_\odot$. Finally, the radius and mass together imply a mean stellar density of $\rho_\star = 18.79 \pm 3.26 \text{ g cm}^{-3}$.

A.3. Stellar parameter comparison

In addition to the methods described above, we used the Python package ISOCHRONES, which calculates stellar parameters from the stellar evolution models. The three methods are not fully independent, as some of them use

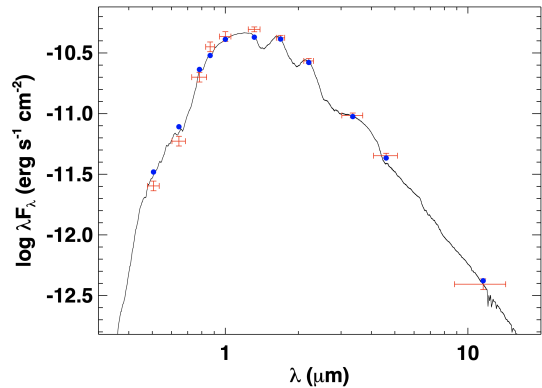


Figure A.16. Spectral energy distribution of TOI-1696. Red symbols represent the observed photometric measurements, where the horizontal bars represent the effective width of the passband. Blue symbols are the model fluxes from the best-fit NextGen atmosphere model (black).

the same relations such as mass derivation from Mann et al. (2019), but comparing three results are useful to confirm the results are robust. The derived stellar parameters agreed within $1 \sim 2\sigma$, as shown in A.1. We pick up the results from the empirical relations as our final stellar parameters in Table 1.

B. CONTAMINATION ANALYSIS

Contamination leads to a decrease in the observed transit depth (the planet appears to be smaller than it truly is), and this effect is achromatic even if the host and the contaminant(s) are of different spectral types. Having simultaneous multicolor photometry allows us to measure possible contamination and consequently

Table A.1. Stellar parameters which were derived from empirical relations (Method 1; Section 3.1.3), SED fitting (Method 2; Section A.2) and ISOCHRONES (Method 3;Section A.3). [†]The resulting posterior is approximately zero and non-Gaussian as a result of using a tight uniform prior close to 0 for numerical reasons.

Parameter	Method 1	Method 2	Method 3
T_{eff} (K)	-	3130 ± 75	3159 ± 40
[Fe/H] (dex)	-	0.2 ± 0.3	$0.232^{+0.035}_{-0.038}$
M_{\star} (M_{\odot})	0.255 ± 0.0066	0.279 ± 0.014	$0.276^{+0.006}_{-0.005}$
R_{\star} (R_{\odot})	0.2775 ± 0.0080	0.280 ± 0.014	0.291 ± 0.005
$\log g$ (cgs)	4.959 ± 0.026	4.990 ± 0.049	$4.955^{+0.008}_{-0.007}$
ρ_{\star} (g cm^{-3})	$16.8^{+1.5}_{-1.4}$	18.0 ± 2.9	$16.282^{+0.598}_{-0.617}$
distance (pc)	65.03 ± 0.36	-	$65.390^{+0.540}_{-0.464}$
Luminosity (L_{\odot})	$0.00711^{+0.00083}_{-0.00075}$	-	-
Av (mag)	0 (fixed)	0 (fixed)	$\sim 0^{\dagger}$
F_{bol} (cgs)	-	$5.19(18) \times 10^{-11}$	-
$M_K s$ (mag)	7.265 ± 0.026	-	-

provides strong constraints on the false positive scenarios discussed in Section 3.6.

Following the methods presented in Parviainen et al. (2020, 2021), we used the physics-based contamination model included in PyTransit v21 to model the light curves using a transit model that includes a light contamination component based on model stellar spectra leveraging multicolor photometry. Fitting the transit+contamination model to MuSCAT3 lightcurves allows us to measure the contamination i' -band¹⁹, the effective temperature of the host ($T_{\text{eff},H}$), and the effective temperature of the contaminant ($T_{\text{eff},C}$). We used normal priors for the period and T_0 based on the results of our transit analysis. We also used normal priors on limb darkening, host effective temperature, and host star density, based on our spectroscopic analysis. Among them, the spectroscopic priors are the most important. Without a limb darkening prior, the transit fit in g-band is boxy perhaps due to the sparse data sampling. Without the $T_{\text{eff},H}$ prior, the posteriors are not well behaved. Without the host ρ_{\star} prior, the model converges to very high values ($\sim 33 \text{ g cm}^{-3}$) which is inconsistent with the results from our previous analyses. The joint and marginal posteriors of the relevant parameters are shown in Figure B.1. Significant levels of blending from sources with effective temperature different from that of the host star are excluded, and also the blending

from sources with $T_{\text{eff},C} \sim T_{\text{eff},H}$ are strongly constrained.

C. HEB SIMULATION

We assumed that each system was composed of the primary star (TOI-1696, Star 1), plus a tertiary companion (Star 3) eclipsing a secondary companion (Star 2) every 2.5 d. For a grid of secondary and tertiary star masses ranging from 0.1 to $0.4 M_{\odot}$, we then calculated the observed maximum eclipse depth caused by Star 3 eclipsing Star 2 in MuSCAT3 g- and z-bands using the following procedure. First, we interpolated L_{\star} and T_{eff} of Star 2 and Star 3 from MIST isochrones given their masses, and the age, metallicity, and mass of Star 1 in Table 1. We then computed the blackbody function of each star given their T_{eff} then convolved it with the transmission functions for each band downloaded from the SVO filter file service²⁰. We then integrated the result using the trapezoidal method and computed the bolometric flux F_{bol} , using the integrated functions above. Using Stefan-Boltzmann law and given T_{eff} and L_{\star} , we computed the component radii and luminosities to derive the eclipse depth.

Figure C.2 shows the HEB configurations that produce eclipse depths in g- (blue) and z-bands (red) that are consistent with the observed depth for two given impact parameters. The lower impact parameter corresponds to the 3- σ lower limit derived from our contamina-

¹⁹ We adopt i' as reference passband for simplicity

²⁰ <http://svo2.cab.inta-csic.es/theory/fps/>

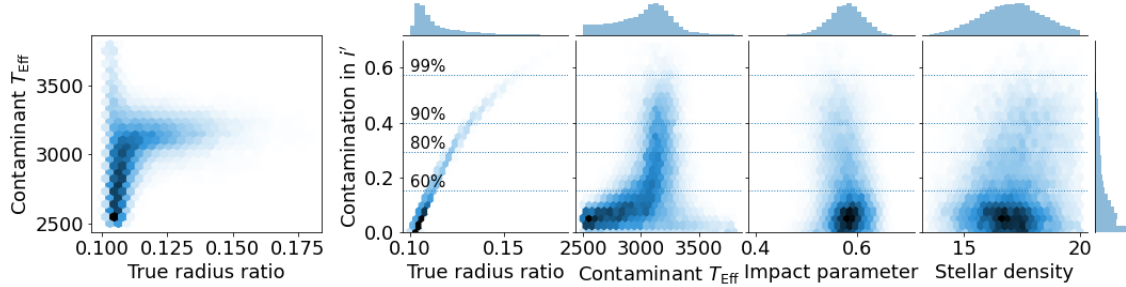


Figure B.1. Joint and marginal posteriors for the key parameters from the transit+contamination modelling of the MuSCAT3 multicolor light curves. Contamination due to sources with significantly different effective temperature than the host is ruled out.

tion analysis while the other impact parameter corresponds to the median value derived in our transit analysis. We confirm that indeed eclipses of an HEB are always deeper in the red than the blue bands (i.e higher m_2/m_1 in z- than g-band) since the eclipsing companions are usually redder than the central star. The important point here is that the HEB configurations that produce eclipses consistent with our observation do not overlap within $1-\sigma$ in g- and z-bands for any reasonable impact parameters. Note also that our contamination analysis constrained possible contaminants to have the same colour as the host star, so only masses very close to TOI-1696 (vertical dashed line in Figure C.2) is allowed. Thus, we can rule out the HEB false positive scenario.

D. VALIDATION WITH VESPA AND TRICERATOPS

VESPA²¹ was originally developed as a tool for statistical validation of planet candidates identified by the *Kepler* mission (e.g. Morton et al. 2016), but has also been used extensively to validate planets from subsequent missions, such as *K2* (e.g. Livingston et al. 2018; de Leon et al. 2021). VESPA compares the likelihood of a planetary scenario to the likelihoods of several astrophysical false positive scenarios involving eclipsing binaries (EBs), hierarchical triple systems (HEBs), background eclipsing binaries (BEBs), and the double-period cases of all these scenarios. The likelihoods and priors for each scenario are based on the shape of the transit signal, the star’s location in the Galaxy, and single-, binary-, and triple-star model fits to the observed photometric and spectroscopic properties of the star generated

using ISOCHRONES. We used the MuSCAT3 lightcurve because of its high SNR and low levels of limb darkening, which provides the best constraint on the transit shape. We also used the Gemini and Palomar contrast curves described in Section 2.6, a maximum aperture radius of $\text{maxrad} = 3''$ (interior to which the transit signal must be produced), and ran the simulation using a population size of $n=10^6$. We computed a formal $\text{FPP} < 1 \times 10^{-6}$ which is small enough to be statistically validate TOI-1696.01 as a planet.

We also used TRICERATOPS²² which is a tool developed to validate TOIs (Giacalone & Dressing 2020; Giacalone et al. 2021) by calculating the Bayesian probabilities of the observed transit originating from several scenarios involving the target star, nearby resolved stars, and hypothetical unresolved stars in the immediate vicinity of the target. These probabilities were then compared to calculate a false positive probability (FPP; the total probability of the transit originating from something other than a planet around the target star) and a nearby false positive probability (NFPP; the total probability of the transit originating from a nearby resolved star). Given our follow-up photometry rules out nearby stars as a potential source of the transit signal, we eliminate all stars except the target in the TRICERATOPS analysis. As an additional constraint, we use the contrast curve from our follow-up speckle imaging as a direct input in TRICERATOPS. For the sake of reliability, we performed the calculation 20 times for the planet candidate and found $\text{FPP}=0.0020$.

²¹ <https://github.com/timothydmorton/VESPA>

²² <https://github.com/stevengiacalone/triceratops>

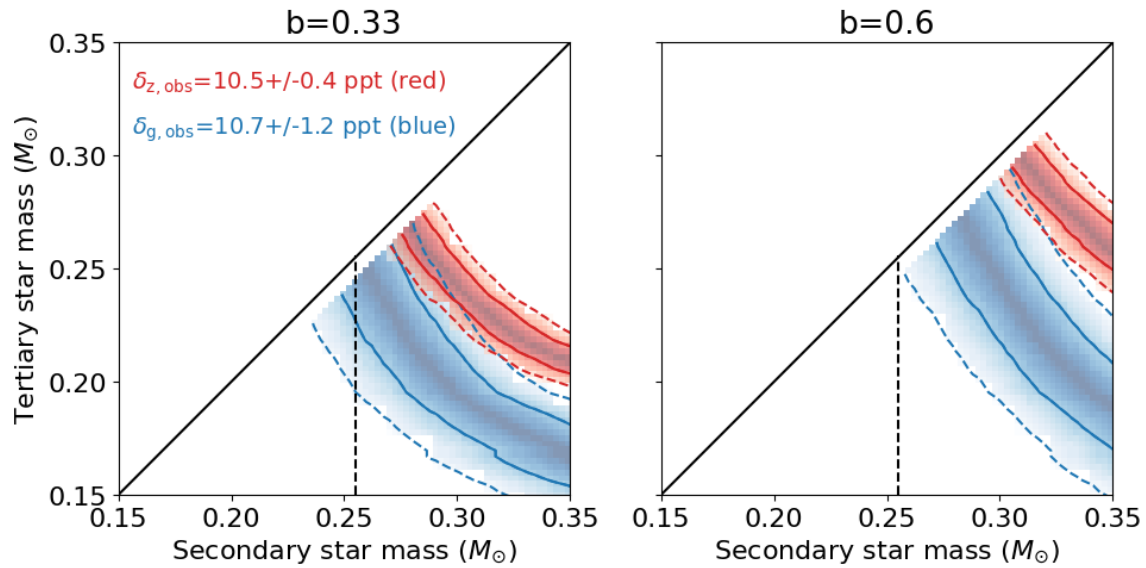


Figure C.2. HEB configurations which produce eclipses in g-band (blue) and z-band (red). The left panel corresponds to the lower limit of the impact parameter and the right for the median value. The solid line and dashed lines correspond to confidence regions that are consistent with the observed depths within 1- and 2- σ , respectively. The vertical dashed line corresponds to the mass of the central star (i.e. TOI-1696). The fact that the red and blue regions do not overlap within 1- σ taking into account impact parameter rules out the HEB as a false positive scenario.

REFERENCES

- 1284 Anderson, O. L., Dubrovinsky, L., Saxena, S. K.,
 1285 & LeBihan, T. 2001, *Geophys. Res. Lett.*, 28,
 1286 399, doi: [10.1029/2000GL008544](https://doi.org/10.1029/2000GL008544)
- 1287 Astropy Collaboration, Robitaille, T. P., Tollerud,
 1288 E. J., et al. 2013, *A&A*, 558, A33,
 1289 doi: [10.1051/0004-6361/201322068](https://doi.org/10.1051/0004-6361/201322068)
- 1290 Astropy Collaboration, Price-Whelan, A. M.,
 1291 Sipőcz, B. M., et al. 2018, *AJ*, 156, 123,
 1292 doi: [10.3847/1538-3881/aabc4f](https://doi.org/10.3847/1538-3881/aabc4f)
- 1293 Bellm, E. C., Kulkarni, S. R., Graham, M. J.,
 1294 et al. 2019, *PASP*, 131, 018002,
 1295 doi: [10.1088/1538-3873/aaecbe](https://doi.org/10.1088/1538-3873/aaecbe)
- 1296 Belokurov, V., Penoyre, Z., Oh, S., et al. 2020,
 1297 *MNRAS*, 496, 1922,
 1298 doi: [10.1093/mnras/staa1522](https://doi.org/10.1093/mnras/staa1522)
- 1299 Borucki, W. J., Koch, D., Basri, G., et al. 2010,
 1300 *Science*, 327, 977, doi: [10.1126/science.1185402](https://doi.org/10.1126/science.1185402)
- 1301 Bouma, L. G., Hartman, J. D., Brahm, R., et al.
 1302 2020, *AJ*, 160, 239,
 1303 doi: [10.3847/1538-3881/abb9ab](https://doi.org/10.3847/1538-3881/abb9ab)
- 1304 Brande, J., Crossfield, I. J. M., Kreidberg, L.,
 1305 et al. 2022, arXiv e-prints, arXiv:2201.04197.
 1306 <https://arxiv.org/abs/2201.04197>
- 1307 Brown, T. M., Baliber, N., Bianco, F. B., et al.
 1308 2013, *PASP*, 125, 1031, doi: [10.1086/673168](https://doi.org/10.1086/673168)
- 1309 Burrows, A., Heng, K., & Nampaisarn, T. 2011,
 1310 *ApJ*, 736, 47, doi: [10.1088/0004-637X/736/1/47](https://doi.org/10.1088/0004-637X/736/1/47)
- 1311 Castro González, A., Díez Alonso, E., Menéndez
 1312 Blanco, J., et al. 2020, *MNRAS*, 499, 5416,
 1313 doi: [10.1093/mnras/staa2353](https://doi.org/10.1093/mnras/staa2353)
- 1314 Charbonneau, D., Berta, Z. K., Irwin, J., et al.
 1315 2009, *Nature*, 462, 891,
 1316 doi: [10.1038/nature08679](https://doi.org/10.1038/nature08679)
- 1317 Claret, A. 2017, *A&A*, 600, A30,
 1318 doi: [10.1051/0004-6361/201629705](https://doi.org/10.1051/0004-6361/201629705)
- 1319 Claret, A., Hauschildt, P. H., & Witte, S. 2012,
 1320 VizieR Online Data Catalog, 354
- 1321 Cointepas, M., Almenara, J. M., Bonfils, X., et al.
 1322 2021, *A&A*, 650, A145,
 1323 doi: [10.1051/0004-6361/202140328](https://doi.org/10.1051/0004-6361/202140328)
- 1324 Collins, K. A., Kielkopf, J. F., Stassun, K. G., &
 1325 Hessman, F. V. 2017, *AJ*, 153, 77,
 1326 doi: [10.3847/1538-3881/153/2/77](https://doi.org/10.3847/1538-3881/153/2/77)
- 1327 Cushing, M. C., Vacca, W. D., & Rayner, J. T.
 1328 2004, *PASP*, 116, 362, doi: [10.1086/382907](https://doi.org/10.1086/382907)
- 1329 Cutri, R. M., Wright, E. L., Conrow, T., et al.
 1330 2021, VizieR Online Data Catalog, II/328
- 1331 de Leon, J. P., Livingston, J., Endl, M., et al.
 1332 2021, arXiv e-prints, arXiv:2108.05621.
 1333 <https://arxiv.org/abs/2108.05621>
- 1334 Dressing, C. D., Hardegree-Ullman, K., Schlieder,
 1335 J. E., et al. 2019, *AJ*, 158, 87,
 1336 doi: [10.3847/1538-3881/ab2895](https://doi.org/10.3847/1538-3881/ab2895)
- 1337 Erkaev, N. V., Kulikov, Y. N., Lammer, H., et al.
 1338 2007, *A&A*, 472, 329,
 1339 doi: [10.1051/0004-6361:20066929](https://doi.org/10.1051/0004-6361:20066929)
- 1340 Foreman-Mackey, D. 2018, *Research Notes of the
 1341 American Astronomical Society*, 2, 31,
 1342 doi: [10.3847/2515-5172/aaaf6c](https://doi.org/10.3847/2515-5172/aaaf6c)
- 1343 Foreman-Mackey, D., Agol, E., Ambikasaran, S.,
 1344 & Angus, R. 2017, *AJ*, 154, 220,
 1345 doi: [10.3847/1538-3881/aa9332](https://doi.org/10.3847/1538-3881/aa9332)
- 1346 Foreman-Mackey, D., Barentsen, G., & Barclay,
 1347 T. 2019, *dfm/exoplanet: exoplanet v0.1.5*,
 1348 doi: [10.5281/zenodo.2587222](https://doi.org/10.5281/zenodo.2587222)
- 1349 Fukui, A., Narita, N., Tristram, P. J., et al. 2011,
 1350 *PASJ*, 63, 287, doi: [10.1093/pasj/63.1.287](https://doi.org/10.1093/pasj/63.1.287)
- 1351 Gagné, J., Mamajek, E. E., Malo, L., et al. 2018,
 1352 *ApJ*, 856, 23, doi: [10.3847/1538-4357/aaae09](https://doi.org/10.3847/1538-4357/aaae09)
- 1353 Giacalone, S., & Dressing, C. D. 2020, arXiv
 1354 e-prints, arXiv:2002.00691.
 1355 <https://arxiv.org/abs/2002.00691>
- 1356 Giacalone, S., Dressing, C. D., Jensen, E. L. N.,
 1357 et al. 2021, *AJ*, 161, 24,
 1358 doi: [10.3847/1538-3881/abc6af](https://doi.org/10.3847/1538-3881/abc6af)
- 1359 Girardi, L., Groenewegen, M. A. T.,
 1360 Hatziminaoglou, E., & da Costa, L. 2005, *A&A*,
 1361 436, 895, doi: [10.1051/0004-6361:20042352](https://doi.org/10.1051/0004-6361:20042352)
- 1362 Guerrero, N. M., Seager, S., Huang, C. X., et al.
 1363 2021, *ApJS*, 254, 39,
 1364 doi: [10.3847/1538-4365/abefc1](https://doi.org/10.3847/1538-4365/abefc1)
- 1365 Hayward, T. L., Brandl, B., Pirger, B., et al.
 1366 2001, *PASP*, 113, 105, doi: [10.1086/317969](https://doi.org/10.1086/317969)
- 1367 Hippke, M., & Heller, R. 2019, *A&A*, 623, A39,
 1368 doi: [10.1051/0004-6361/201834672](https://doi.org/10.1051/0004-6361/201834672)
- 1369 Hirano, T., Kuzuhara, M., Kotani, T., et al. 2020,
 1370 *PASJ*, 72, 93, doi: [10.1093/pasj/psaa085](https://doi.org/10.1093/pasj/psaa085)
- 1371 Hirano, T., Livingston, J. H., Fukui, A., et al.
 1372 2021, *AJ*, 162, 161,
 1373 doi: [10.3847/1538-3881/ac0fdc](https://doi.org/10.3847/1538-3881/ac0fdc)
- 1374 Hoffman, M. D., & Gelman, A. 2014, *Journal of
 1375 Machine Learning Research*, 15, 1593
- 1376 Howell, S. B., Everett, M. E., Sherry, W., Horch,
 1377 E., & Ciardi, D. R. 2011, *AJ*, 142, 19,
 1378 doi: [10.1088/0004-6256/142/1/19](https://doi.org/10.1088/0004-6256/142/1/19)

- 1379 Ionov, D. E., & Shematovich, V. I. 2015, Solar
 1380 System Research, 49, 339,
 1381 doi: [10.1134/S0038094615050056](https://doi.org/10.1134/S0038094615050056)
- 1382 Ishikawa, H. T., Aoki, W., Kotani, T., et al. 2020,
 1383 PASJ, 72, 102, doi: [10.1093/pasj/psaa101](https://doi.org/10.1093/pasj/psaa101)
- 1384 Ishikawa, H. T., Aoki, W., Hirano, T., et al. 2022,
 1385 AJ, 163, 72, doi: [10.3847/1538-3881/ac3ee0](https://doi.org/10.3847/1538-3881/ac3ee0)
- 1386 Jackson, A. P., Davis, T. A., & Wheatley, P. J.
 1387 2012, MNRAS, 422, 2024,
 1388 doi: [10.1111/j.1365-2966.2012.20657.x](https://doi.org/10.1111/j.1365-2966.2012.20657.x)
- 1389 Jenkins, J. M. 2002, ApJ, 575, 493,
 1390 doi: [10.1086/341136](https://doi.org/10.1086/341136)
- 1391 Jenkins, J. M., & et al. 2020, Kepler Science
 1392 Document KSCI-19081-003, Kepler Science
 1393 Document KSCI-19081-003
- 1394 Jenkins, J. M., Chandrasekaran, H., McCauliff,
 1395 S. D., et al. 2010, in Society of Photo-Optical
 1396 Instrumentation Engineers (SPIE) Conference
 1397 Series, Vol. 7740, Software and
 1398 Cyberinfrastructure for Astronomy, ed. N. M.
 1399 Radziwill & A. Bridger, 7740D,
 1400 doi: [10.1117/12.856764](https://doi.org/10.1117/12.856764)
- 1401 Jenkins, J. S., Díaz, M. R., Kurtovic, N. T., et al.
 1402 2020, Nature Astronomy, 4, 1148,
 1403 doi: [10.1038/s41550-020-1142-z](https://doi.org/10.1038/s41550-020-1142-z)
- 1404 Kanodia, S., Wolfgang, A., Stefansson, G. K.,
 1405 Ning, B., & Mahadevan, S. 2019, ApJ, 882, 38,
 1406 doi: [10.3847/1538-4357/ab334c](https://doi.org/10.3847/1538-4357/ab334c)
- 1407 Karki, B. B., Wentzcovitch, R. M., de Gironcoli,
 1408 S., & Baroni, S. 2000, PhRvB, 62, 14750,
 1409 doi: [10.1103/PhysRevB.62.14750](https://doi.org/10.1103/PhysRevB.62.14750)
- 1410 Kempton, E. M. R., Bean, J. L., Louie, D. R.,
 1411 et al. 2018, PASP, 130, 114401,
 1412 doi: [10.1088/1538-3873/aadf6f](https://doi.org/10.1088/1538-3873/aadf6f)
- 1413 Kipping, D. M. 2013, MNRAS, 435, 2152,
 1414 doi: [10.1093/mnras/stt1435](https://doi.org/10.1093/mnras/stt1435)
- 1415 Kochanek, C. S., Shappee, B. J., Stanek, K. Z.,
 1416 et al. 2017, PASP, 129, 104502,
 1417 doi: [10.1088/1538-3873/aa80d9](https://doi.org/10.1088/1538-3873/aa80d9)
- 1418 Kotani, T., Tamura, M., Nishikawa, J., et al.
 1419 2018, in Society of Photo-Optical
 1420 Instrumentation Engineers (SPIE) Conference
 1421 Series, Vol. 10702, Ground-based and Airborne
 1422 Instrumentation for Astronomy VII, ed. C. J.
 1423 Evans, L. Simard, & H. Takami, 1070211,
 1424 doi: [10.1117/12.2311836](https://doi.org/10.1117/12.2311836)
- 1425 Kuzuhara, M., Hirano, T., Kotani, T., et al. 2018,
 1426 in Society of Photo-Optical Instrumentation
 1427 Engineers (SPIE) Conference Series, Vol. 10702,
 1428 Ground-based and Airborne Instrumentation
 1429 for Astronomy VII, ed. C. J. Evans, L. Simard,
 1430 & H. Takami, 1070260, doi: [10.1117/12.2311832](https://doi.org/10.1117/12.2311832)
- 1431 Li, J., Tenenbaum, P., Twicken, J. D., et al. 2019,
 1432 PASP, 131, 024506,
 1433 doi: [10.1088/1538-3873/aaf44d](https://doi.org/10.1088/1538-3873/aaf44d)
- 1434 Livingston, J. H., Crossfield, I. J. M., Petigura,
 1435 E. A., et al. 2018, AJ, 156, 277,
 1436 doi: [10.3847/1538-3881/aae778](https://doi.org/10.3847/1538-3881/aae778)
- 1437 Lopez, E. D. 2017, MNRAS, 472, 245,
 1438 doi: [10.1093/mnras/stx1558](https://doi.org/10.1093/mnras/stx1558)
- 1439 Luger, R., Agol, E., Foreman-Mackey, D., et al.
 1440 2019, AJ, 157, 64,
 1441 doi: [10.3847/1538-3881/aae8e5](https://doi.org/10.3847/1538-3881/aae8e5)
- 1442 Mann, A. W., Brewer, J. M., Gaidos, E., Lépine,
 1443 S., & Hilton, E. J. 2013, AJ, 145, 52,
 1444 doi: [10.1088/0004-6256/145/2/52](https://doi.org/10.1088/0004-6256/145/2/52)
- 1445 Mann, A. W., Feiden, G. A., Gaidos, E.,
 1446 Boyajian, T., & von Braun, K. 2015, ApJ, 804,
 1447 64, doi: [10.1088/0004-637X/804/1/64](https://doi.org/10.1088/0004-637X/804/1/64)
- 1448 Mann, A. W., Gaidos, E., Mace, G. N., et al.
 1449 2016, ApJ, 818, 46,
 1450 doi: [10.3847/0004-637X/818/1/46](https://doi.org/10.3847/0004-637X/818/1/46)
- 1451 Mann, A. W., Dupuy, T., Kraus, A. L., et al.
 1452 2019, ApJ, 871, 63,
 1453 doi: [10.3847/1538-4357/aaf3bc](https://doi.org/10.3847/1538-4357/aaf3bc)
- 1454 Masci, F. J., Laher, R. R., Rusholme, B., et al.
 1455 2019, PASP, 131, 018003,
 1456 doi: [10.1088/1538-3873/aae8ac](https://doi.org/10.1088/1538-3873/aae8ac)
- 1457 Mazeh, T., Holczer, T., & Faigler, S. 2016, A&A,
 1458 589, A75, doi: [10.1051/0004-6361/201528065](https://doi.org/10.1051/0004-6361/201528065)
- 1459 McCully, C., Volgenau, N. H., Harbeck, D.-R.,
 1460 et al. 2018, in Society of Photo-Optical
 1461 Instrumentation Engineers (SPIE) Conference
 1462 Series, Vol. 10707, Software and
 1463 Cyberinfrastructure for Astronomy V, ed. J. C.
 1464 Guzman & J. Ibsen, 107070K,
 1465 doi: [10.1117/12.2314340](https://doi.org/10.1117/12.2314340)
- 1466 Morton, T. D. 2015, VESPA: False positive
 1467 probabilities calculator.
 1468 <http://ascl.net/1503.011>
- 1469 Morton, T. D., Bryson, S. T., Coughlin, J. L.,
 1470 et al. 2016, ApJ, 822, 86,
 1471 doi: [10.3847/0004-637X/822/2/86](https://doi.org/10.3847/0004-637X/822/2/86)
- 1472 Muñoz, J. L., & Evans, D. W. 2014,
 1473 Astronomische Nachrichten, 335, 367,
 1474 doi: [10.1002/asna.201312045](https://doi.org/10.1002/asna.201312045)

- 1475 Murgas, F., Astudillo-Defru, N., Bonfils, X., et al.
 1476 2021, A&A, 653, A60,
 1477 doi: [10.1051/0004-6361/202140718](https://doi.org/10.1051/0004-6361/202140718)
- 1478 Narita, N., Fukui, A., Kusakabe, N., et al. 2015,
 1479 Journal of Astronomical Telescopes,
 1480 Instruments, and Systems, 1, 045001,
 1481 doi: [10.1117/1.JATIS.1.4.045001](https://doi.org/10.1117/1.JATIS.1.4.045001)
- 1482 Narita, N., Fukui, A., Yamamoto, T., et al. 2020,
 1483 in Society of Photo-Optical Instrumentation
 1484 Engineers (SPIE) Conference Series, Vol.
 1485 11447, Society of Photo-Optical
 1486 Instrumentation Engineers (SPIE) Conference
 1487 Series, 114475K, doi: [10.1117/12.2559947](https://doi.org/10.1117/12.2559947)
- 1488 Newton, E. R., Charbonneau, D., Irwin, J., et al.
 1489 2014, AJ, 147, 20,
 1490 doi: [10.1088/0004-6256/147/1/20](https://doi.org/10.1088/0004-6256/147/1/20)
- 1491 —. 2022, tellrv: Radial velocities for
 1492 low-resolution NIR spectra.
 1493 <http://ascl.net/2201.007>
- 1494 Nocedal, J., & Wright, S. J. 2006, Numerical
 1495 Optimization, 2nd edn. (New York, NY, USA:
 1496 Springer)
- 1497 Owen, J. E., & Wu, Y. 2017, ApJ, 847, 29,
 1498 doi: [10.3847/1538-4357/aa890a](https://doi.org/10.3847/1538-4357/aa890a)
- 1499 Parviainen, H., Palle, E., Zapatero-Osorio, M. R.,
 1500 et al. 2020, A&A, 633, A28,
 1501 doi: [10.1051/0004-6361/201935958](https://doi.org/10.1051/0004-6361/201935958)
- 1502 —. 2021, A&A, 645, A16,
 1503 doi: [10.1051/0004-6361/202038934](https://doi.org/10.1051/0004-6361/202038934)
- 1504 Pecaut, M. J., & Mamajek, E. E. 2013, ApJS,
 1505 208, 9, doi: [10.1088/0067-0049/208/1/9](https://doi.org/10.1088/0067-0049/208/1/9)
- 1506 Rasmussen, C. E., & Williams, C. K. I. 2005,
 1507 Gaussian Processes for Machine Learning
 1508 (Adaptive Computation and Machine
 1509 Learning) (The MIT Press)
- 1510 Rayner, J. T., Toomey, D. W., Onaka, P. M.,
 1511 et al. 2003, PASP, 115, 362,
 1512 doi: [10.1086/367745](https://doi.org/10.1086/367745)
- 1513 Reid, I. N., Brewer, C., Brucato, R. J., et al.
 1514 1991, PASP, 103, 661, doi: [10.1086/132866](https://doi.org/10.1086/132866)
- 1515 Ricker, G. R., Winn, J. N., Vanderspek, R., et al.
 1516 2015, Journal of Astronomical Telescopes,
 1517 Instruments, and Systems, 1, 014003,
 1518 doi: [10.1117/1.JATIS.1.1.014003](https://doi.org/10.1117/1.JATIS.1.1.014003)
- 1519 Rogers, L. A. 2015, ApJ, 801, 41,
 1520 doi: [10.1088/0004-637X/801/1/41](https://doi.org/10.1088/0004-637X/801/1/41)
- 1521 Salpeter, E. E., & Zapsolsky, H. S. 1967, Physical
 1522 Review, 158, 876,
 1523 doi: [10.1103/PhysRev.158.876](https://doi.org/10.1103/PhysRev.158.876)
- 1524 Salvatier, J., Wiecki, T. V., & Fonnesbeck, C.
 1525 2016, PeerJ Computer Science, 2, e55
- 1526 Saumon, D., Chabrier, G., & van Horn, H. M.
 1527 1995, ApJS, 99, 713, doi: [10.1086/192204](https://doi.org/10.1086/192204)
- 1528 Scott, N. J. 2019, in AAS/Division for Extreme
 1529 Solar Systems Abstracts, Vol. 51, AAS/Division
 1530 for Extreme Solar Systems Abstracts, 330.15
- 1531 Seager, S., Kuchner, M., Hier-Majumder, C. A.,
 1532 & Militzer, B. 2007, ApJ, 669, 1279,
 1533 doi: [10.1086/521346](https://doi.org/10.1086/521346)
- 1534 Shematovich, V. I., Ionov, D. E., & Lammer, H.
 1535 2014, A&A, 571, A94,
 1536 doi: [10.1051/0004-6361/201423573](https://doi.org/10.1051/0004-6361/201423573)
- 1537 Skrutskie, M. F., Cutri, R. M., Stiening, R., et al.
 1538 2006, AJ, 131, 1163, doi: [10.1086/498708](https://doi.org/10.1086/498708)
- 1539 Smith, J. C., Stumpe, M. C., Van Cleve, J. E.,
 1540 et al. 2012, PASP, 124, 1000,
 1541 doi: [10.1086/667697](https://doi.org/10.1086/667697)
- 1542 Stassun, K. G., Collins, K. A., & Gaudi, B. S.
 1543 2017, AJ, 153, 136,
 1544 doi: [10.3847/1538-3881/aa5df3](https://doi.org/10.3847/1538-3881/aa5df3)
- 1545 Stassun, K. G., & Torres, G. 2016, AJ, 152, 180,
 1546 doi: [10.3847/0004-6256/152/6/180](https://doi.org/10.3847/0004-6256/152/6/180)
- 1547 —. 2021, ApJL, 907, L33,
 1548 doi: [10.3847/2041-8213/abdaad](https://doi.org/10.3847/2041-8213/abdaad)
- 1549 Stassun, K. G., Oelkers, R. J., Pepper, J., et al.
 1550 2018, AJ, 156, 102,
 1551 doi: [10.3847/1538-3881/aad050](https://doi.org/10.3847/1538-3881/aad050)
- 1552 Stumpe, M. C., Smith, J. C., Catanzarite, J. H.,
 1553 et al. 2014, PASP, 126, 100,
 1554 doi: [10.1086/674989](https://doi.org/10.1086/674989)
- 1555 Stumpe, M. C., Smith, J. C., Van Cleve, J. E.,
 1556 et al. 2012, PASP, 124, 985,
 1557 doi: [10.1086/667698](https://doi.org/10.1086/667698)
- 1558 Szabó, G. M., & Kiss, L. L. 2011, ApJL, 727,
 1559 L44, doi: [10.1088/2041-8205/727/2/L44](https://doi.org/10.1088/2041-8205/727/2/L44)
- 1560 Tamura, M., Suto, H., Nishikawa, J., et al. 2012,
 1561 in Society of Photo-Optical Instrumentation
 1562 Engineers (SPIE) Conference Series, Vol. 8446,
 1563 Ground-based and Airborne Instrumentation
 1564 for Astronomy IV, ed. I. S. McLean, S. K.
 1565 Ramsay, & H. Takami, 84461T,
 1566 doi: [10.1117/12.925885](https://doi.org/10.1117/12.925885)
- 1567 Tody, D. 1993, in Astronomical Society of the
 1568 Pacific Conference Series, Vol. 52, Astronomical
 1569 Data Analysis Software and Systems II, ed.
 1570 R. J. Hanisch, R. J. V. Brissenden, &
 1571 J. Barnes, 173
- 1572 Toledo-Padrón, B., González Hernández, J. I.,
 1573 Rodríguez-López, C., et al. 2019, MNRAS, 488,
 1574 5145, doi: [10.1093/mnras/stz1975](https://doi.org/10.1093/mnras/stz1975)

- 1575 Twicken, J. D., Catanzarite, J. H., Clarke, B. D.,
1576 et al. 2018, PASP, 130, 064502,
1577 doi: [10.1088/1538-3873/aab694](https://doi.org/10.1088/1538-3873/aab694)
- 1578 Vacca, W. D., Cushing, M. C., & Rayner, J. T.
1579 2003, PASP, 115, 389, doi: [10.1086/346193](https://doi.org/10.1086/346193)
- 1580 Watson, A. J., Donahue, T. M., & Walker,
1581 J. C. G. 1981, Icarus, 48, 150,
1582 doi: [10.1016/0019-1035\(81\)90101-9](https://doi.org/10.1016/0019-1035(81)90101-9)
- 1583 Weiss, L. M., & Marcy, G. W. 2014, ApJL, 783,
1584 L6, doi: [10.1088/2041-8205/783/1/L6](https://doi.org/10.1088/2041-8205/783/1/L6)
- 1585 Wells, R. D., Rackham, B. V., Schanche, N., et al.
1586 2021, A&A, 653, A97,
1587 doi: [10.1051/0004-6361/202141277](https://doi.org/10.1051/0004-6361/202141277)
- 1588 West, R. G., Gillen, E., Bayliss, D., et al. 2019,
1589 MNRAS, 486, 5094,
1590 doi: [10.1093/mnras/stz1084](https://doi.org/10.1093/mnras/stz1084)
- 1591 Zeng, L., & Sasselov, D. 2013, PASP, 125, 227,
1592 doi: [10.1086/669163](https://doi.org/10.1086/669163)